Research Square

Preprints are preliminary reports that have not undergone peer review.
They should not be considered conclusive, used to inform clinical practice,
or referenced by the media as validated information.

Sertoli Tfeb and Tfe3 Redundantly Sustain Spermatogenesis via Cycs-Mediated Mitochondrial Bioenergetics

Hongyong Zhang

zhanghongyong13@mails.ucas.ac.cn

Central People's Hospital of Zhanjiang, Guangdong Medical University https://orcid.org/0000-0001-5585-1206

Zechen Li

Central People's Hospital of Zhanjiang, Guangdong Medical University Zhanjiang Central Hospital

Xiaoyu Li

Guangdong Provincial Key Laboratory of Autophagy and Major Chronic Non-Communicable Diseases, Affiliated Hospital of Guangdong Medical University https://orcid.org/0000-0002-0241-6152

Ruigao Song

Shanxi Bethune Hospital

Yifei Wu

Guangdong Medical University

Wenlu Wei

Guangdong Medical University Zhanjiang Central Hospital

Wen-Long Lei

State Key Laboratory of Stem Cell and Reproductive Biology, Institute of Zoology, Chinese Academy of Sciences, Beijing https://orcid.org/0000-0003-0562-5125

Wei Yue

Fertility Preservation Lab, Reproductive Medicine Center, Guangdong Second Provincial General Hospital, Guangzhou

Xiaoning Cheng

Central People's Hospital of Zhanjiang, Guangdong Medical University

Hongxia Zhao

Central People's Hospital of Zhanjiang, Guangdong Medical University

Qing-Yuan Sun

Guangdong Second Provincial General Hospital https://orcid.org/0000-0002-0148-2414

Lijuan Pang

Central People's Hospital of Zhanjiang, Guangdong Medical University

Donghui Zhang

Guangdong Medical University Zhanjiang Central Hospital https://orcid.org/0000-0002-6208-6984

Article

Keywords:

Posted Date: November 16th, 2026

DOI: https://doi.org/10.21203/rs.3.rs-11212749/v1

License: This work is licensed under a Creative Commons Attribution 4.0 International License.
Read Full License

Additional Declarations: (Not answered)

Sertoli Tfeb and Tfe3 Redundantly Sustain Spermatogenesis via Cycs-Mediated Mitochondrial Bioenergetics

Zechen Li[1,†], Xiaoyu Li[2,†], Ruigao Song[3,†], Yifei Wu[4,†], Wenlu Wei[5], Wen-Long Lei[6], Wei Yue[7], Xiaoning Cheng[5], Hongxia Zhao[5], Qing-Yuan Sun[8], Lijuan Pang[9,*], Donghui Zhang[9,*], Hongyong Zhang[9,*]

[1]Precision Clinical Laboratory, Central People's Hospital of Zhanjiang, Guangdong Medical University, Zhanjiang, 524045, China.

[2]Institute of Nephrology, Key Laboratory of Prevention and Management of Chronic Kidney Disease of Zhanjiang City, Guangdong Provincial Key Laboratory of Autophagy and Major Chronic Non-communicable Diseases, Affiliated Hospital of Guangdong Medical University, Zhanjiang, 524001, China.

[3]Shanxi Bethune Hospital, Shanxi Academy of Medical Sciences, Third Hospital of ShanxiMedical-University, Tongji Shanxi Hospital, Taiyuan, 030032, China.

[4]College of Pharmacy, Zhanjiang Central Hospital, Guangdong Medical University, Dongguan, 523808, China.

[5]Zhanjiang Institute of Clinical Medicine, Central People's Hospital of Zhanjiang, Guangdong Medical University, Zhanjiang, 524045, China.

[6]Inner Mongolia Key Laboratory for Molecular Regulation of the Cell, State Key Laboratory of Reproductive Regulation & Breeding of Grassland Livestock, College of Life Sciences, Inner Mongolia University, Hohhot, 010020, China.

[7]College of Life Science, Shenyang Normal University, Shenyang, 110034, China.

[8]Guangzhou Key Laboratory of Metabolic Diseases and Reproductive Health, Guangdong-Hong Kong Metabolism & Reproduction Joint Laboratory, Reproductive Medicine Center, Guangdong Second Provincial General Hospital, Guangzhou, 510317, China.

[9]Zhanjiang Institute of Clinical Medicine, Central People's Hospital of Zhanjiang, Guangdong Medical University, Zhanjiang, 524045, China. Electronic address: zhanghongyong13@mails.ucas.ac.cn; Zdh2014@pku.edu.cn; plj_123456@gdmu.edu.cn.

†These authors contributed equally.

*These authors jointly supervised this work: Hongyong Zhang, Donghui Zhang, Lijuan Pang.

Abstract

Sertoli cells provide essential metabolic and bioenergetic support to developing germ cells, thereby sustaining male fertility. However, the transcriptional networks that safeguard somatic mitochondrial homeostasis, and their potential involvement in idiopathic male infertility, remain largely unexplored. Here, we report that the MiT/TFE transcription factors Tfeb and Tfe3 function redundantly to maintain Sertoli cell function; their concurrent deletion in mice results in severe oligo-astheno-teratozoospermia (OAT) and profound subfertility. Single-cell transcriptomic, metabolomic, and ultrastructural analyses reveal that simultaneous Tfeb and Tfe3 deficiency collapses mitochondrial bioenergetic homeostasis in Sertoli cells, characterized by a depleted tricarboxylic acid (TCA) cycle and markedly reduced ATP production. Mechanistically, by integrating CUT&Tag and transcriptomic profiling, we identify *Cycs* (encoding cytochrome c) as a direct transcriptional target. Both Tfeb and Tfe3 bind to discrete *cis*-regulatory elements within the *Cycs* promoter to drive its expression, which is required to maintain respiratory chain integrity. Together, these findings establish a crucial Tfeb/Tfe3-Cycs-ATP signaling axis that couples somatic mitochondrial energetics to germ cell development, providing a conceptual framework and potential therapeutic targets for male reproductive disorders.

Keywords: Energy metabolism; Mitochondrial; OAT; Tfeb/Tfe3; Cycs

Introduction

Male reproductive health has emerged as a growing biomedical concern, underscored by evidence of declining semen quality across multiple populations [1, 2, 3]. Oligo-astheno-teratozoospermia (OAT), characterized by reduced sperm count, impaired motility, and abnormal morphology, remains one of the leading causes of male infertility [4, 5, 6, 7]. Although genetic factors contribute to OAT pathogenesis, the underlying etiology remains highly heterogeneous. Spermatogenesis is governed by a complex regulatory network involving thousands of genes, rendering its genetic architecture intrinsically multifactorial [8, 9, 10]. Consequently, the mechanistic basis of OAT remains incompletely understood, highlighting the need for robust experimental models and systematic dissection of the molecular pathways that govern spermatogenic failure.

Spermatogenesis is a highly orchestrated developmental process that occurs within the seminiferous tubules of the testis, where germ cells undergo sequential mitotic and meiotic divisions to produce haploid spermatozoa [11, 12, 13]. This process depends intimately on coordinated interaction between germ cells and Sertoli cells, which serve as essential somatic “nurse” cells within the seminiferous epithelium [14, 15, 16]. Sertoli cells provide structural scaffolding, metabolic substrates, and paracrine signals required for germ cell development [14, 17, 18, 19]. They also mediate clearance of apoptotic germ cells and maintain the blood-testis barrier, thereby establishing an immune-privileged microenvironment [20, 21]. These diverse functions impose substantial metabolic demands on Sertoli cells, necessitating tightly regulated bioenergetic homeostasis.

Mitochondria serve as central bioenergetic organelles that sustain ATP production through oxidative phosphorylation. Their functional integrity is maintained through a dynamic balance of mitochondrial biogenesis, fission-fusion events, and selective mitophagy [22, 23]. Disruption of this balance can lead to bioenergetic failure or accumulation of damaged organelles, both of which have been implicated in spermatogenic arrest and idiopathic male infertility [20, 24, 25, 26, 27, 28]. Given the high energetic demands of Sertoli cells, maintenance of mitochondrial homeostasis is

essential for the completion of spermiogenesis. However, the upstream transcriptional mechanisms that coordinate mitochondrial function in Sertoli cells remain largely undefined.

Transcription factor EB (Tfeb) and transcription factor E3 (Tfe3), members of the MiT/TFE family of basic helix-loop-helix leucine zipper transcription factors, are well established master regulators of lysosomal biogenesis and autophagy [29, 30, 31, 32, 33, 34, 35, 36]. Beyond these canonical roles, accumulating evidence indicates that Tfeb and Tfe3 participate in broader metabolic processes, including glucose homeostasis and lipid metabolism [37, 38, 39]. Dysregulation of Tfeb/Tfe3 has been linked to impaired mitochondrial function, reduced ATP production, and altered metabolic flux in multiple cellular contexts [40]. Despite these advances, their functional roles in testicular Sertoli cells, particularly in the regulation of mitochondrial bioenergetics during spermatogenesis, remain unexplored.

In this study, we demonstrate that Tfeb and Tfe3 are co-expressed in murine Sertoli cells and function cooperatively to maintain male fertility. Using a Sertoli cell-specific double knockout model, we show that concurrent deletion of Tfeb and Tfe3 leads to impaired spermatogenesis, characterized by reduced sperm count, impaired motility, and abnormal morphology, closely resembling human OAT. Integrative multi-omics analyses reveal that loss of Tfeb/Tfe3 disrupts mitochondrial bioenergetic homeostasis, resulting in decreased ATP production. Mechanistically, we identify *Cycs*, an essential electron shuttle sustaining proton gradient-coupled ATP synthesis [41, 42], as a direct transcriptional target of Tfeb and Tfe3. Together, our findings define a previously unrecognized Tfeb/Tfe3-Cycs-ATP axis that is essential for Sertoli cell function and male reproductive competence.

Result

Single deletion of *Tfeb* or *Tfe3* does not impair male reproductive capacity

To investigate the roles of Tfeb and Tfe3 in spermatogenesis, we generated Sertoli cell-specific knockout mice using the *AMH*-Cre driver (Fig. S1A and Fig. S2A). Efficient deletion of Tfeb and Tfe3 was confirmed by immunoblotting and immunofluorescence

(Fig. S1B-S1C and Fig. S2B-S2C). Notably, single-knockout mice developed normally and exhibited no overt reproductive defects. Fertility assays revealed comparable pregnancy rates and litter sizes between knockout and control groups (Fig. S1D and Fig. S2D). Consistent with these findings, histological examination showed intact spermatogenesis and normal sperm architecture (Fig. S1E and Fig. S2E). These results suggest functional redundancy between Tfeb and Tfe3 in maintaining Sertoli cell function and male fertility.

Combined deletion of *Tfeb* and *Tfe3* impairs male fertility

Given the potential compensatory relationship between Tfeb and Tfe3 [43, 44, 45, 46, 47], we generated Sertoli cell-specific double-knockout (DKO) mice. Efficient ablation of both proteins was confirmed at the protein level (Fig.1A-1C and Fig. S3A-S3B). In marked contrast to single knockouts, DKO males exhibited substantially reduced fertility, with significantly lower pregnancy rates and smaller litter sizes (Fig. 1D). Histological analysis revealed intact testicular architecture but a marked reduction in mature spermatozoa within the epididymis (Fig. 1E-1F). Detailed examination revealed abnormal sperm aggregation in the caput epididymidis and the presence of non-sperm cells in the cauda epididymidis, indicating defects in sperm maturation and transport (Fig. 1F). These data demonstrate that Tfeb and Tfe3 function cooperatively to sustain male fertility.

Loss of *Tfeb* and *Tfe3* causes oligo-astheno-teratozoospermia in mice

To further characterize the reproductive defects in DKO mice, we performed detailed phenotypic analysis. PAS staining indicated that early meiotic progression was largely unaffected (Fig. 2A); however, pronounced abnormalities were observed during the elongation phase of spermatid development (Fig. 2D). Quantitative analysis revealed a significant reduction in sperm concentration and impaired total and progressive motility (Fig. 2C). Morphological assessment identified severe structural defects, including malformed heads and coiled or bent flagella (Fig. 2D). Scanning electron microscopy (SEM) confirmed aberrant head morphology and disrupted flagellar architecture (Fig. 2E). Collectively, these defects recapitulate the defining features of oligo-astheno-teratozoospermia (OAT), establishing the DKO model as a relevant system for

investigating male infertility.

Tfeb and *Tfe3* deficiency disrupts sperm flagellar biogenesis

To elucidate the molecular basis of these defects, we performed single-cell RNA sequencing (scRNA-seq) on testes from DKO and control mice (Fig. 3A). Unsupervised clustering resolved all major cell types, indicating preservation of overall cellular composition (Fig. 3B-3C). However, quantitative assessment revealed a reduced proportion of Sertoli cells and a marked depletion of spermatogonia in DKO testes (Fig. 3D). Transcriptomic analysis of spermatids showed significant downregulation of genes involved in cilium organization, flagellar assembly, and spermatid differentiation (Fig. 4A-4B). Transmission electron microscopy (TEM) confirmed these findings, revealing disorganized axonemal structures, defective head-tail coupling, and abnormal mitochondrial morphology (Fig. 4C-4F). These results indicate that loss of Tfeb/Tfe3 disrupts spermatid differentiation programs, particularly those dependent on high energy demand.

Ablation of *Tfeb* and *Tfe3* engenders metabolic dyshomeostasis in Sertoli cells

We next examined how Tfeb and Tfe3 loss affects Sertoli cell function. While blood-testis barrier (BTB) dysfunction is a well-established cause of spermatogenic failure [48, 49, 50], ultrastructural analysis confirmed intact BTB structural in DKO mice (Fig. S3C), indicating that the observed defects were not structural. Gene Ontology analysis of RNA-seq data revealed significant enrichment of pathways related to mitochondrial function and energy metabolism among downregulated genes in DKO Sertoli cells (Fig. 5A). Given the energy-intensive nature of spermatogenesis, we next investigated whether Tfeb/Tfe3 deficiency affects Sertoli cell metabolism. Untargeted metabolomic profiling of DKO and control testes identified 20 metabolites with significantly altered abundance (Fig. 5B and Fig. S4A). Notably, four of the 10 downregulated metabolites in the DKO group were tricarboxylic acid (TCA) cycle intermediates (Fig. 5C-5D). Correspondingly, ATP measurements demonstrated significantly reduced energy production in DKO tissues (Fig. 5E). These findings establish that Tfeb and Tfe3 are essential for maintaining metabolic homeostasis in Sertoli cells.

Cycs is a central target regulated by Tfeb and Tfe3

To identify the downstream effectors of Tfeb/Tfe3, we integrated CUT&Tag profiling and transcriptomic analysis. This integrative approach identified a subset of genes directly regulated by Tfeb/Tfe3 that are enriched for metabolic processes and membrane-bounded organelle functions (Fig. 6A). Functional assays confirmed that mitochondrial membrane potential was reduced and ROS levels were elevated in DKO Sertoli cells (Fig. 6B-6C, and Fig. S4B-S4D), consistent with mitochondrial dysfunction. Western blot analysis further revealed a marked reduction in mitochondrial protein abundance in DKO Sertoli cells (Fig. 6D and Fig. S4E). Overlap analysis identified 287 shared genes between downregulated DEGs in DKO Sertoli cells and Tfeb target genes (Fig. 6E). Integration with CUT&Tag enrichment scores highlighted *Cycs* as a primary candidate (Fig. 6F). CUT&Tag and ChIP-qPCR analyses confirmed direct binding of Tfeb to the *Cycs* promoter (Fig. 6G and Fig. S4F). Reporter assays demonstrated that both Tfeb and Tfe3 activate *Cycs* transcription through distinct *cis*-regulatory elements, and mutation of these binding sites substantially reduced transcriptional activity (Fig. 6H and Fig. S4G). These data establish *Cycs* as a direct transcriptional target of Tfeb/Tfe3 and identify it as a central mediator of mitochondrial bioenergetics in Sertoli cells. In summary, our findings delineate a mechanistic axis wherein Tfeb and Tfe3, operating in testicular Sertoli cells, transcriptionally govern *Cycs* to preserve mitochondrial bioenergetics and ATP biosynthesis, the disruption of which consequently elicits compromised spermatozoal quality and diminished male fecundity (Fig. 7); this delineation not only furnishes a molecular framework for the clinical diagnosis of male infertility but also nominates a tractable therapeutic target for future pharmacological exploitation.

Discussion

Our findings establish an unconventional transcriptional paradigm wherein the MiT/TFE family members, Tfeb and Tfe3, act as core arbiters of mitochondrial bioenergetics within the testicular niche. In addition to their well-characterized functions in lysosomal biogenesis and autophagy [51, 52, 53], these transcription factors function cooperatively to maintain Sertoli cell metabolic integrity, a prerequisite

for male reproductive competence. The absence of a phenotype in single-knockout mice, contrasted with the pronounced spermiogenic defects in DKO animals, reveals a considerable degree of functional redundancy. This genetic buffering likely ensures that the somatic support network of the seminiferous epithelium remains resilient against isolated transcriptional disruptions under physiological conditions.

Sertoli cell-specific deletion of Tfeb and Tfe3 reproduces key features of human oligo-astheno-teratozoospermia (OAT), providing a genetic platform to investigate the metabolic basis of male infertility. Notably, gross testicular architecture and blood-testis barrier integrity were preserved in DKO mice, allowing us to decouple structural maintenance from metabolic support functions. Single-cell transcriptomics clarified this distinction: while early germ cell progression through meiosis proceeded normally, late-stage spermiogenic processes requiring substantial energy input, including flagellar assembly and cytoskeletal remodeling, were selectively impaired. This stage-specific vulnerability underscores the dependence of elongating spermatids on somatic ATP supply.

At the mechanistic level, our multi-omics analysis points to a bioenergetic deficit driven by impaired oxidative phosphorylation. The profound depletion of TCA cycle intermediates and reduced ATP production in DKO Sertoli cells indicate an energy deficit that affects germ cell development non-cell-autonomously. We identify *Cycs* as the crucial node linking this transcriptional-metabolic axis. Beyond its established function as an electron carrier in the respiratory chain [54, 55], cytochrome c serves as a rate-limiting metabolic gatekeeper dictated by Tfeb and Tfe3. Our binding and site-directed mutagenesis data demonstrate that Tfeb and Tfe3 directly bind to discrete *cis*-regulatory elements within the *Cycs* promoter; disruption of these binding sites abolishes transcriptional activation and compromises mitochondrial respiratory capacity, establishing a direct causal trajectory from elite transcription factors to organelle performance.

The Tfeb/Tfe3-Cycs-ATP regulatory axis described here links somatic cell metabolism to germ cell morphogenesis. Given the evolutionary conservation of the MiT/TFE network, similar regulatory mechanisms may operate in other metabolically demanding

tissues, such as the central nervous system or the beating myocardium, where support cell metabolism influences parenchymal cell viability. From a clinical perspective, the phenotypic concordance between our DKO model and human OAT suggests that genetic or epigenetic alterations within the Tfeb/Tfe3-Cycs axis may contribute to a subset of cases currently classified as idiopathic male infertility. Therapeutic approaches targeting this axis, whether through modulation of MiT/TFE activity or the metabolic resuscitation of Cycs expression, may offer potential strategies for addressing mitochondrial deficits in male reproductive disorders.

While this study delineates a clear causal trajectory, several questions remain open for future investigation. First, although *Cycs* stands out as a high-priority, non-redundant effector, it operates within a broader, Tfeb/Tfe3-orchestrated transcriptional landscape; the subtle contributions of other co-regulated mitochondrial targets warrant future proteomic dissection. Second, characterizing the precise, real-time metabolic flux between Sertoli cells and developing spermatids *in vivo* presents a significant technical challenge. Future studies deploying cell-type-specific genetic rescue and intravital metabolic imaging will refine the spatiotemporal dynamics of this metabolic exchange. In summary, our work findings define a seminal transcriptional-metabolic axis whereby Tfeb and Tfe3 cooperatively fuel Sertoli cell mitochondrial function, thereby supporting spermiogenesis and male fertility. These insights provide both a conceptual blueprint and an experimental framework for further investigation into the metabolic basis of male reproductive disorders and may inform future therapeutic strategies.

Methods

Ethics approval and animal care

All animal experimental procedures were approved by the Institutional Animal Care and Use Committee (IACUC) of the Central People's Hospital of Zhanjiang (Approval ID: KYSB-DW-2025055-01) and performed in strict accordance with institutional guidelines for the care and use of laboratory animals. Mice were housed in a specific pathogen-free (SPF) barrier facility under standard environmental conditions (22 ± 3°C; 50–70% humidity) with a 12 h light/dark cycle. Animals had ad libitum access to standard laboratory chow and water.

Generation of Sertoli cell-specific knockout mice and genotyping

Tfeb$^{flox/flox}$ and *Tfe3*$^{flox/flox}$ mice were obtained from GemPharmatech Corporation (Nanjing, China). To generate Sertoli cell-specific conditional knockout (cKO) mice, *Tfeb*$^{flox/flox}$ or *Tfe3*$^{flox/flox}$ females were crossed with *AMH-Cre* transgenic males to yield *AMH-Cre; Tfeb/Tfe3*$^{+/flox}$ females. These female offspring were subsequently backcrossed with *Tfeb/Tfe3*$^{flox/flox}$ males to generate conditional single-knockout (*AMH-Cre; Tfeb*$^{flox/flox}$, *AMH-Cre; Tfe3*$^{flox/flox}$) and double-knockout (*AMH-Cre; Tfeb*$^{flox/flox}$*; Tfe3*$^{flox/flox}$) mice, designated as DKO mice. Cre-negative littermates served as controls. Genotyping was performed on genomic DNA extracted from tail biopsies using PCR (primers listed in Table S1).

Fertility assessment

To evaluate reproductive capacity, 8-week-old DKO (n = 12) and control (n = 12) males were individually housed with two wild-type (WT) females of proven fertility. Vaginal plugs were checked daily at 08:00, and litter sizes were recorded.

Histological analysis and immunofluorescence staining

Testes and epididymides from 8-week-old mice were fixed in 4% paraformaldehyde (PFA) at 4°C for 24 h. Tissues were subsequently dehydrated through a graded ethanol series, cleared in xylene, and embedded in paraffin blocks. Sagittal sections (5 μm) were stained with Hematoxylin and Eosin (H&E) or Periodic Acid-Schiff (PAS)-hematoxylin (Beyotime, Shanghai, China, Cat #C0142S). Histopathological images were acquired using a light microscope (Nikon, Tokyo, Japan).

For immunofluorescence, sections underwent heat-induced antigen retrieval and blocking with 5% BSA in PBS for 1 h at room temperature, and were incubated overnight at 4°C with the following primary antibodies: anti-Tfeb (1:200, Bethyl Laboratories, Cat #A303-673A), anti-Tfe3 (1:200, Sigma-Aldrich, Cat #HPA023881), anti-Gata4 (1:100, Santa Cruz Biotechnology, Cat #sc25310), anti-MVH (1:300, Abcam, Cat #ab27591), and anti-α-tubulin (1:500, Sigma-Aldrich, Cat #F2168). Acrosome development was visualized using fluorescein isothiocyanate (FITC)-conjugated Peanut Agglutinin (PNA, 1:400, Thermo Fisher Scientific, Cat #L21409).

Sections were incubated with Alexa Fluor 488- or Cy3-conjugated secondary antibodies (1:500, Invitrogen) for 1 h at room temperature. Nuclei were counterstained with Hoechst 33342 for 10 min. Images were acquired using a confocal microscope (Nikon, Tokyo, Japan).

Epididymal sperm quality evaluation

Spermatozoa were collected from the cauda epididymis of 8-week-old mice and incubated in pre-warmed PBS at 37°C for 30 min. Sperm concentration, total motility, and progressive motility were assessed using a Computer-Assisted Sperm Analysis (CASA) system (IVOS II, Hamilton Thorne, Beverly, MA, USA). Morphological analysis was performed on smears stained with Papanicolaou EA50 (Saitong, Cat #PS0386) under a 100× oil immersion objective (Nikon, Tokyo, Japan).

Electron microscopy

For Scanning Electron Microscopy (SEM), sperm were centrifuged at 5,000 rpm for 5 min, washed twice with PBS, and fixed in 2.5% glutaraldehyde in 0.1 M sodium cacodylate buffer (pH 7.4) overnight at 4°C. Fixed sperm were rinsed three times with PBS, dehydrated through a graded ethanol gradient (30%, 50%, 75%, 95%, and 100%), and dried using a carbon dioxide critical-point dryer. Samples were mounted on stubs, sputter-coated with gold-palladium using an ionic sprayer (Eiko E-1020, Hitachi, Japan), and examined via an S-3400 scanning electron microscope (Hitachi, Japan).

For Transmission Electron Microscopy (TEM), intact testes or sperm pellets were fixed in 2.5% glutaraldehyde overnight, post-fixed with 1.5% osmium tetroxide for 2 h at 4°C, and dehydrated through graded ethanol. Tissues were embedded in Epon 812 resin. Ultrathin sections (70-90 nm) were prepared, mounted on copper grids, stained with uranyl acetate and lead citrate, and examined under a Quanta 10 transmission electron microscope (FEI Co., Hillsboro, OR, USA).

Western blot analysis

Total protein extraction from frozen testes or isolated Sertoli cells was executed using RIPA lysis buffer (Thermo Fisher Scientific, Cat #89901) supplemented with protease and phosphatase inhibitor cocktails. Protein concentrations were quantified using a

BCA Protein Assay Kit (Beyotime, Cat #P0010). Equal amounts of protein (30 μg) were boiled in 5×SDS loading buffer (Beyotime, Cat #P0015L) at 100°C for 10 min, separated via SDS-PAGE, and transferred onto polyvinylidene difluoride (PVDF) membranes (Millipore, Cat #IPFL00010). Membranes were blocked with 5% skimmed milk in TBST for 1 h at 37°C and probed overnight at 4°C with primary antibodies against Tfeb (Bethyl, Cat #A303-673A), Tfe3 (Sigma-Aldrich, Cat #HPA023881), Cycs (Abcam, Cat #ab133504), Tomm20 (BD Biosciences, Cat #612278), Cox4 (Cell Signaling Technology, Cat #4844s), β-actin (Proteintech, Cat #20536-1-AP), and Gapdh (Proteintech, Cat #20536-1-AP). After incubation with horseradish peroxidase (HRP)-conjugated secondary antibodies for 1 h at room temperature, protein bands were visualized using an enhanced chemiluminescence system and quantified using an iBright™ Imaging System (Thermo Fisher Scientific, Waltham, MA, USA).

Intracellular reactive oxygen species (ROS) and mitochondrial membrane potential (MMP) assays

Intracellular ROS levels in primary Sertoli cells were evaluated using a ROS Assay Kit (Beyotime, Cat #C1062S). Cells were incubated with 10 mM dichlorofluorescein diacetate (DCFH-DA) in serum-free medium at 37°C for 20 min in the dark. After three washes with PBS, green fluorescence intensity was analyzed via laser scanning confocal microscopy (Nikon, Tokyo, Japan).

MMP was monitored using the ratiometric fluorescent probe JC-1 (Invitrogen, Cat #M34152). Sertoli cells were cultured with 2 mM JC-1 for 30 min at 37°C in the dark, washed twice, and imaged. Highly energized mitochondria exhibit red fluorescence, whereas depolarized mitochondria exhibit green fluorescence. The ratio of red-to-green fluorescence intensity was quantified using ImageJ software (NIH, Bethesda, MD, USA).

Quantification of testicular ATP content

Testicular ATP levels were measured using an Enhanced ATP Assay Kit (Beyotime, Cat #S0027) via a luminometric approach. Briefly, tissues were homogenized in lysis buffer and centrifuged at 12,000 g for 5 min at 4°C. Supernatants were mixed with the ATP

detection working solution. Luminescence was measured, and absolute ATP concentrations were calculated based on a concurrent 6-point standard curve (0.01 to 10 μM) and normalized to total protein content.

Chromatin Immunoprecipitation (ChIP)-qPCR

ChIP assays were performed on primary Sertoli cells. Cells were cross-linked with 1% formaldehyde for 15 min at room temperature, followed by quenching with glycine. Chromatin was isolated and sheared into 400-700 bp fragments using a Sonicator (Scientz, Ningbo, China). Immunoprecipitation was conducted overnight at 4°C using 3 μg of anti-Tfeb antibody (Bethyl, Cat #A303-673A) or normal rabbit IgG (Proteintech, Cat #30000-0-AP) complexed with pre-blocked Protein A/G magnetic beads (Thermo Fisher Scientific, Cat #10004D). Following sequential washes and decross-linking at 65°C, enriched DNA fragments were purified utilizing a Gel DNA Extraction Mini Kit (Vazyme, Nanjing, China, Cat #DC301-01). Quantitative PCR (qPCR) was performed to determine the enrichment at target promoters. Primers are detailed in Table S1.

Dual-Luciferase reporter assay

Plasmids containing the wild-type Cycs promoter (pGL4-WT-Cycs, NM_007808.5) or site-directed mutational variants (pGL4-M1-Cycs, pGL4-M2-Cycs, pGL4-M3-Cycs, and pGL4-M1+M2+M3-Cycs), alongside expression vectors pcDNA3.1-Tfeb and pcDNA3.1-Tfe3, were synthesized by Tsingke Biotechnology (Beijing, China; sequence details in Table S2). HEK293T cells were maintained in DMEM supplemented with 10% FBS. Upon reaching 70% confluence in 12-well plates, cells were co-transfected with 100 ng of reporter plasmid, 500 ng of expression vector (or empty vector control), and 50 ng of pGL4.74-hRluc-TK (Promega, Madison, WI, USA) as an internal normalization control, utilizing Lipofectamine 3000 (Invitrogen). At 24 h post-transfection, Firefly and Renilla luciferase activities were determined sequentially using the Dual-Luciferase Reporter Assay System (Promega) on a GloMax 96 microplate luminometer (Promega).

Untargeted metabolomics analysis

Testicular tissues from 8-week-old DKO and control mice (n = 7 biological replicates

per group) were snap-frozen in liquid nitrogen. Metabolomic profiling was performed via a 600MRM LC-MS/MS platform (Biotree, Shanghai, China). Briefly, 25 mg of tissue was homogenized at 35 Hz for 4 min with 1500 μL of an acetonitrile/methanol/water mixture (2:2:1, v/v/v) containing isotopic internal standards. Homogenates were sonicated in an ice-water bath for 5 min (repeated 3 times) and incubated at -40°C for 2 h. Supernatants collected via centrifugation (12,000 rpm, 4°C, 15 min) were dried down using a vacuum concentrator. Dried residues were reconstituted in 120 μL of 60% acetonitrile, centrifuged, and the final supernatants were analyzed on an Agilent 1290 UHPLC system coupled to an AB Sciex Triple Quad 6500 Plus mass spectrometer. Raw data processing and quantification were executed via SCIEX Analyst Work Station Software (v1.7.3) and BIOTREE BioBud (v2.0.3). Differentially expressed metabolites were defined by a Variable Importance in the Projection (VIP) score > 1.0 and a Student's t-test $p < 0.05$.

Single-cell RNA sequencing (scRNA-seq) and data processing

Testicular tissues from 2-month-old DKO and control littermates were enzymatically dissociated into single-cell suspensions. Cell viability was determined to be > 75% via trypan blue exclusion. Cell suspensions were loaded into the Chromium Controller (10×Genomics, Pleasanton, CA, USA) to generate Gel Bead-in-Emulsions (GEMs). Libraries were constructed using the Chromium Single Cell 3′ Library & Gel Bead Kit v3 (10×Genomics, Cat #120237) and sequenced on the Illumina NovaSeq 6000 platform (Novogene, Beijing, China) to a depth of 20,000 read pairs per cell.

Raw FASTQ files were processed using the Cell Ranger pipeline (v7.1, 10×Genomics) with alignment to the mouse reference genome (mm10) using the STAR aligner. The filtered unique molecular identifier (UMI) matrices were analyzed using the Seurat R package (v4.3.0). Standard quality control filtered out low-quality cells based on the following criteria: 200-6500 expressed genes per cell, mitochondrial UMI counts < 25%, and hemoglobin gene expression < 5%. Potential doublets were predicted and eliminated utilizing DoubletFinder. Gene Ontology (GO) enrichment analysis of differentially expressed genes (DEGs) was implemented, with Benjamini-Hochberg adjusted $p < 0.05$ considered statistically significant.

CUT&Tag library preparation and bioinformatic analysis

CUT&Tag assays were performed on testicular tissues from 8-week-old littermates. Tissues were mechanically dissociated using a Dounce homogenizer and filtered through a 40 μm strainer to yield single cells. Approximately 1×10^5 cells were bound to Concanavalin A-coated magnetic beads and permeabilized with digitonin. Samples were incubated overnight at 4°C with anti-Tfeb antibody (Bethyl, Cat #A303-673A) or normal rabbit IgG control (Proteintech, Cat #30000-0-AP), followed by incubation with secondary antibodies. Cells were then treated with Hyperactive pA-Tn5 Transposase (Vazyme) pre-loaded with adapters. Tagmentation was activated by adding Mg^{2+}-containing buffer at 37°C for 1 h. Extracted DNA fragments were amplified by PCR with indexed primers, and size selection (200-700 bp) was carried out using SPRI beads. Libraries were sequenced on an Illumina platform.

Raw reads were quality-checked via FastQC and trimmed using Trimmomatic. Clean reads were aligned to the mm10 genome using Bowtie2. Enriched peaks were called using MACS2 (v2.2.7.1) against the IgG baseline. Peak annotation and motif discovery were performed using HOMER (v4.11). Genomic signal tracks were generated via deepTools and visualized using the Integrative Genomics Viewer (IGV).

Statistical analysis

Data are presented as the mean ± standard error of the mean (s.e.m.) from at least three independent biological replicates. Statistical comparisons between two experimental groups were analyzed using the two-tailed unpaired Student's t-test in GraphPad Prism software (v11.0, GraphPad Software, San Diego, CA, USA). Differences were considered statistically significant at $p < 0.05$. Significance levels are graphically indicated as follows: *$P < 0.05$, **$P < 0.01$, ***$P < 0.001$.

Data availability

The scRNA-seq and CUT&Tag raw datasets derived from murine whole testes have been deposited in the National Genomics Data Center (accession no. CRA044342) in FASTQ format. Any additional supporting data generated during this research can be made available by the corresponding author following a justifiable request.

Acknowledgements

We sincerely thank Prof. Jianguo Zhao from Chinese Academy of Sciences for the kind comments. We also thank the personnel of the Molecular Biology Laboratory, the SPF Laboratory Animal Center, and the Biomedical Imaging Platform at the Zhanjiang Institute of Clinical Medicine for their assistance with data collection and analysis. This work was supported by National Natural Science Foundation of China (82301863, 82000647), the Guangdong Basic and Applied Basic Research Foundation (2025A1515012236), the Open Research Fund of the National Center for Protein Sciences at Peking University in Beijing (KF-202503), the Central People's Hospital of Zhanjiang Startup Project of Doctor Scientific Research (2022A13, 2021A04, 2020A05) and Zhanjiang Science and Technology Project (2022A01104), the Discipline Construction Fund of Central People's Hospital of Zhanjiang (2022A15, 2025A04).

Author contributions

H.Y.Z., D.H.Z., and L.J.P. designed the study and secured funding. H.Y.Z., Z.C.L., and W.L.W. were responsible for mouse husbandry and genotyping. Z.C.L., X.Y.L., R.G.S., and Y.F.W. performed the experiments with assistance from W.L.L., W.Y., and H.X.Z. The initial draft of the manuscript was written by H.Y.Z., and Q.Y.S. contributed to its revision. All authors provided critical feedback on the manuscript and approved the final version.

Competing interests

The authors declare no competing interests.

References

1. Inhorn MC, Patrizio P. Infertility around the globe: new thinking on gender, reproductive technologies and global movements in the 21st century. *Human reproduction update* 2015, **21**(4)**:** 411-426.

2. Aponte PM, Gutierrez-Reinoso MA, Garcia-Herreros M. Bridging the Gap: Animal Models in Next-Generation Reproductive Technologies for Male Fertility Preservation. *Life (Basel)* 2023, **14**(1).

3. Kaltsas A, Dimitriadis F, Zachariou D, Zikopoulos A, Symeonidis EN, Markou E*, et al.* From Diagnosis to Treatment: Comprehensive Care by Reproductive Urologists in Assisted Reproductive Technology. *Medicina* 2023, **59**(10).

4. Jiao SY, Yang YH, Chen SR. Molecular genetics of infertility: loss-of-function mutations in humans and corresponding knockout/mutated mice. *Human reproduction update* 2021, **27**(1)**:** 154-189.

5. Li S, Zhang Z, Xie L, Zhao Y, Chen H, Zhang S*, et al.* Novel bi-allelic DNAH3 variants cause oligoasthenoteratozoospermia. *Front Endocrinol (Lausanne)* 2024, **15:** 1462509.

6. Weiten R, M VB, Huerta M, Nestler T, Heidenreich A, Storz E*, et al.* Altered Endothelin Receptor Expression in Idiopathic Male Infertility: A Potential Therapeutic Target. *Urol Res Pract* 2025, **51**(1)**:** 27-32.

7. Liu H, Zhang H, Qin G, Song T, Liu X, Wen Z*, et al.* Loss of Cep135 causes oligoasthenoteratozoospermia and male infertility in mice. *Cellular and Molecullar Life Sciences* 2025, **82**(1)**:** 117.

8. Nakamura T, Yao R, Ogawa T, Suzuki T, Ito C, Tsunekawa N*, et al.* Oligo-asthenoteratozoospermia in mice lacking Cnot7, a regulator of retinoid X receptor beta. *Nat Genet* 2004, **36**(5)**:** 528-533.

9. Matzuk MM, Lamb DJ. Genetic dissection of mammalian fertility pathways. *Nature cell biology* 2002, **4 Suppl:** s41-49.

10. Mak V, Jarvi KA. The genetics of male infertility. *J Urol* 1996, **156**(4)**:** 1245-1256; discussion 1256-1247.

11. Cheng CY, Mruk DD. An intracellular trafficking pathway in the seminiferous epithelium regulating spermatogenesis: a biochemical and molecular perspective. *Crit Rev Biochem Mol Biol* 2009, **44**(5)**:** 245-263.

12. Griswold MD. Spermatogenesis: The Commitment to Meiosis. *Physiol Rev* 2016, **96**(1)**:** 1-17.

13. Yan H, Chen J, Qing E, Li X, Wang W, Ling Z*, et al.* Developmental variations of the reproductive organs of ganders from different goose breeds and the underlying mechanisms. *Poult Sci* 2024, **103**(11)**:** 104233.

14. Nishimura H, L'Hernault SW. Spermatogenesis. *Current biology : CB* 2017, **27**(18)**:** R988-R994.

15. Chen J, Han C. In vivo functions of miRNAs in mammalian spermatogenesis. *Front Cell Dev Biol* 2023, **11:** 1154938.

16. Higuchi K, Matsumura T, Akiyama H, Kanai Y, Ogawa T, Sato T. Sertoli cell replacement in explanted mouse testis tissue supporting host spermatogenesisdagger. *Biology of Reproduction* 2021, **105**(4)**:** 934-943.

17. Ni FD, Hao SL, Yang WX. Multiple signaling pathways in Sertoli cells: recent findings in spermatogenesis. *Cell death & disease* 2019, **10**(8)**:** 541.

18. Wang JM, Li ZF, Yang WX, Tan FQ. Follicle-stimulating hormone signaling in Sertoli cells: a licence to the early stages of spermatogenesis. *Reproductive biology and endocrinology : RB&E* 2022, **20**(1)**:** 97.

19. Kang K, Ma YD, Liu SQ, Huang RW, Chen JJ, An LL*, et al.* SARS-CoV-2 Structural Proteins Modulated Blood-Testis Barrier-Related Proteins through Autophagy in the Primary Sertoli Cells. *Viruses* 2023, **15**(6).

20. Li S, Kong L, Liang J, Ma T. [Research progress on glycolipid metabolism of Sertoli cell in the development of spermatogenic cell]. *Zhejiang da xue xue bao Yi xue ban = Journal of Zhejiang University Medical sciences* 2025, **54**(2)**:** 257-265.

21. Xiong W, Wang H, Wu H, Chen Y, Han D. Apoptotic spermatogenic cells can be energy sources for Sertoli cells. *Reproduction* 2009, **137**(3)**:** 469-479.

22. Tam ZY, Gruber J, Halliwell B, Gunawan R. Context-Dependent Role of Mitochondrial Fusion-Fission in Clonal Expansion of mtDNA Mutations. *PLoS Comput Biol* 2015, **11**(5)**:** e1004183.

23. Xian H, Liou YC. Functions of outer mitochondrial membrane proteins: mediating the crosstalk between mitochondrial dynamics and mitophagy. *Cell death and differentiation* 2021, **28**(3)**:** 827-842.

24. Ma T, Xia Y, Wang B, Yang F, Ding J, Wu J*, et al.* Environmentally relevant perinatal exposure to DBP accelerated spermatogenesis by promoting the glycolipid metabolism of Sertoli cells in male offspring mice. *Toxicol Lett* 2023, **377:** 16-28.

25. Gorga A, Rindone GM, Dasso ME, Centola CL, Pellizzari EH, Camberos MC*, et al.* Simultaneous regulation of lactate production and fatty acid metabolism by Resveratrol in rat Sertoli cells. *Biochimie* 2023, **208:** 75-85.

26. Luo D, Zhang M, Su X, Liu L, Zhou X, Zhang X*, et al.* High fat diet impairs spermatogenesis by regulating glucose and lipid metabolism in Sertoli cells. *Life Sci* 2020, **257:** 118028.

27. Xie X, Sun L, Duan Y, Lv Z, Yao X, Wang C*, et al.* SRSF2 in Sertoli cells is essential for testicular development and spermatogenesis in mice. *FASEB journal : official publication of the Federation of American Societies for Experimental Biology* 2023, **37**(5)**:** e22918.

28. Wu D, Pandupuspitasari NS, Zhang K, Tang Y, Khan FA, Li H*, et al.* Cytoskeletal orchestration of glucose uptake in Sertoli cell to support efferocytosis of apoptotic germ cells. *Biochimica et biophysica acta Molecular cell research* 2023, **1870**(4)**:** 119434.

29. Haq R, Fisher DE. Biology and clinical relevance of the micropthalmia family of transcription factors in human cancer. *Journal of clinical oncology : official journal of the American Society of Clinical Oncology* 2011, **29**(25)**:** 3474-3482.

30. Settembre C, Di Malta C, Polito VA, Garcia Arencibia M, Vetrini F, Erdin S*, et al.* TFEB links autophagy to lysosomal biogenesis. *Science* 2011, **332**(6036)**:** 1429-1433.

31. Ong AJS, Bladen CE, Tigani TA, Karamalakis AP, Evason KJ, Brown KK*, et al.* The KEAP1-NRF2 pathway regulates TFEB/TFE3-dependent lysosomal biogenesis. *Proceedings of the National Academy of Sciences of the United States of America* 2023, **120**(22)**:** e2217425120.

32. Nezich CL, Wang C, Fogel AI, Youle RJ. MiT/TFE transcription factors are activated during mitophagy downstream of Parkin and Atg5. *The Journal of cell biology* 2015, **210**(3)**:** 435-450.

33. Paquette M, El-Houjeiri L, L CZ, Puustinen P, Blanchette P, Jeong H*, et al.* AMPK-dependent phosphorylation is required for transcriptional activation of TFEB and TFE3. *Autophagy* 2021, **17**(12)**:** 3957-3975.

34. Cai R, Scott O, Ye G, Le T, Saran E, Kwon W*, et al.* Pressure sensing of lysosomes enables control of TFEB responses in macrophages. *Nature cell biology* 2024, **26**(8)**:** 1247-1260.

35. Zhu X, Wu Y, Li Y, Zhou X, Watzlawik JO, Chen YM*, et al.* The nutrient-sensing Rag-GTPase complex in B cells controls humoral immunity via TFEB/TFE3-dependent mitochondrial fitness. *Nature Communications* 2024, **15**(1)**:** 10163.

36. Curnock R, Yalci K, Palmfeldt J, Jaattela M, Liu B, Carroll B. TFEB-dependent lysosome biogenesis is required for senescence. *The EMBO journal* 2023, **42**(9)**:** e111241.

37. Pasquier A, Pastore N, D'Orsi L, Colonna R, Esposito A, Maffia V*, et al.* TFEB and TFE3 control glucose homeostasis by regulating insulin gene expression. *The EMBO journal* 2023, **42**(21)**:** e113928.

38. Settembre C, De Cegli R, Mansueto G, Saha PK, Vetrini F, Visvikis O*, et al.* TFEB controls cellular lipid metabolism through a starvation-induced autoregulatory loop. *Nature cell biology* 2013, **15**(6)**:** 647-658.

39. Yoo J, Jeong IK, Ahn KJ, Chung HY, Hwang YC. Fenofibrate, a PPARalpha agonist, reduces hepatic fat accumulation through the upregulation of TFEB-mediated lipophagy. *Metabolism* 2021, **120:** 154798.

40. Bellese G, Tagliatti E, Gagliani MC, Santamaria S, Arnaldi P, Falletta P*, et al.* Neratinib is a TFEB and TFE3 activator that potentiates autophagy and unbalances energy metabolism in ERBB2+ breast cancer cells. *Biochemical pharmacology* 2023, **213:** 115633.

41. Zhou Z, Arroum T, Luo X, Kang R, Lee YJ, Tang D*, et al.* Diverse functions of cytochrome c in cell death and disease. *Cell death and differentiation* 2024, **31**(4)**:** 387-404.

42. Song X, Zhou Z, Liu J, Li J, Yu C, Zeh HJ*, et al.* Cytosolic cytochrome c represses ferroptosis. *Cell metabolism* 2025, **37**(6)**:** 1326-1343 e1310.

43. Zibetti C. Molecular Determinants of the Human Retinal Pigment Epithelium Cell Fate and Potential Pharmacogenomic Targets for Precision Medicine. *Int J Mol Sci* 2025, **26**(12).

44. Pastore N, Brady OA, Diab HI, Martina JA, Sun L, Huynh T*, et al.* TFEB and TFE3 cooperate in the regulation of the innate immune response in activated macrophages. *Autophagy* 2016, **12**(8)**:** 1240-1258.

45. Pastore N, Vainshtein A, Klisch TJ, Armani A, Huynh T, Herz NJ*, et al.* TFE3 regulates whole-body energy metabolism in cooperation with TFEB. *EMBO molecular medicine* 2017, **9**(5)**:** 605-621.

46. Chao X, Wang S, Zhao K, Li Y, Williams JA, Li T*, et al.* Impaired TFEB-Mediated Lysosome Biogenesis and Autophagy Promote Chronic Ethanol-Induced Liver Injury and Steatosis in Mice. *Gastroenterology* 2018, **155**(3)**:** 865-879 e812.

47. Raben N, Puertollano R. TFEB and TFE3: Linking Lysosomes to Cellular Adaptation to Stress. *Annu Rev Cell Dev Biol* 2016, **32:** 255-278.

48. Kong X, Wang X, Xia Q, Hu Q, Yu W, Huang Q*, et al.* Unveiling the nexus between environmental exposures and testicular damages: revelations from autophagy and oxidative stress imbalance. *Cell Death Discov* 2025, **11**(1)**:** 258.

49. Lie PP, Cheng CY, Mruk DD. Interleukin-1alpha is a regulator of the blood-testis barrier. *FASEB journal : official publication of the Federation of American Societies for Experimental Biology* 2011, **25**(4)**:** 1244-1253.

50. Kheradmand F, Nourmohammadi I, Ahmadi-Faghih MA, Firoozrai M, Modarressi MH. Zinc and low-dose of cadmium protect sertoli cells against toxic-dose of cadmium: The role of metallothionein. *Iran J Reprod Med* 2013, **11**(6)**:** 487-494.

51. Zheng B, Qian F, Wang X, Wang Y, Zhou B, Fang L. Neddylation activated TRIM25 desensitizes triple-negative breast cancer to paclitaxel via TFEB-mediated autophagy. *J Exp Clin Cancer Res* 2024, **43**(1)**:** 177.

52. Yang C, Zhu Z, Tong BC, Iyaswamy A, Xie WJ, Zhu Y*, et al.* A stress response p38 MAP kinase inhibitor SB202190 promoted TFEB/TFE3-dependent autophagy and lysosomal biogenesis independent of p38. *Redox Biol* 2020, **32:** 101445.

53. Dang TT, Back SH. Translation Inhibitors Activate Autophagy Master Regulators TFEB and TFE3. *Int J Mol Sci* 2021, **22**(21).

54. Xue X, Hou J, Zhang Z, Yang Z, Chang L, Yang Z*, et al.* TDP-43-driven alternative splicing of UQCRC2 modulates mitochondrial bioenergetics. *Biol Direct* 2026, **21**(1).

55. Martinez-Ramirez I, Carrillo-Garcia A, Contreras-Paredes A, Ortiz-Sanchez E, Cruz-Gregorio A, Lizano M. Regulation of Cellular Metabolism by High-Risk Human Papillomaviruses. *Int J Mol Sci* 2018, **19**(7).

Figure Legends

Fig. 1 Sertoli cell-specific deletion of Tfeb and Tfe3 impairs male fertility. A Immunoblot analysis of Tfeb and Tfe3 expression in postnatal day 60 (P60) control (Ctrl) and double knockout (DKO) mouse testes. Gapdh was used as a loading control. Genotype definitions: Ctrl, *Tfeb*$^{fl/fl}$; *Tfe3*$^{fl/fl}$; DKO, *Amh*-Cre; *Tfeb*$^{fl/fl}$; *Tfe3*$^{fl/fl}$. **B** and **C** Representative immunofluorescence images of Tfeb (**B**) and Tfe3 (**C**) in P60 Ctrl and DKO testis sections. Sertoli cells were co-labeled with Gata4 (red), and nuclei were counterstained with DAPI (blue). White dashed circles indicate Tfeb- or Tfe3-deficient Sertoli cells. Scale bars, 50 μm. **D** Pregnancy rate (left) and average litter size (right) of wild-type female mice vited with 8-week-old Ctrl or DKO

males (n ≥ 6 males per genotype). Data are presented as mean ± s.e.m. *$P < 0.05$, **$P < 0.01$, ***$P < 0.001$ by two-tailed Student's t-test. **E** Representative hematoxylin and eosin (H&E) staining of seminiferous tubules from P60 Ctrl and DKO mice. Scale bar, 50 μm. **F** Histological analysis of the caput (top) and cauda (bottom) epididymides from Ctrl and DKO mice. Black arrows indicate mature spermatozoa in the DKO caput or non-sperm cellular debris in the DKO cauda. Scale bars, 50 μm.

Fig. 2 Spermatid differentiation and morphological defects in the absence of Tfeb and Tfe3. A Periodic acid–Schiff (PAS) and hematoxylin staining of P60 testis sections from Ctrl and DKO mice. Roman numerals indicate the stages of the seminiferous epithelial cycle. Cell types are labeled as follows: A, type A spermatogonia; IN, intermediate spermatogonia; B, type B spermatogonia; L, leptotene spermatocytes; Z, zygotene spermatocytes; P, pachytene spermatocytes; M, metaphase cells; RS, round spermatids; ES, elongating spermatids. Scale bar, 10 μm. **B** Immunofluorescence analysis of spermatids at sequential manchette developmental stages, co-stained with α-tubulin (red) and peanut agglutinin (PNA, green; acrosome marker). Scale bar, 5 μm. **C** Computer-assisted sperm analysis (CASA) parameters of spermatozoa isolated from the cauda epididymidis of Ctrl and DKO mice. Data are presented as mean ± s.e.m. *$P < 0.05$, **$P < 0.01$, ***$P < 0.001$ by two-tailed Student's t-test. **D** and **E** Representative Papanicolaou staining (**D**) and scanning electron microscopy (SEM) images (**E**) of spermatozoa from Ctrl and DKO mice. Phenotypes include absent, short, bent, or coiled flagella, and malformed heads. Scale bars: 10 μm (**D**); 10 μm (**E**, top); 2 μm (**E**, bottom).

Fig. 3 Single-cell transcriptomic landscape of adult control and double-knockout testes. A Schematic flowchart illustrating the single-cell RNA sequencing (scRNA-seq) experimental design, workflow, and downstream computational analysis pipeline. **B** Uniform Manifold Approximation and Projection (UMAP) plot showing 39,236 integrated single-cell transcriptomes from adult mouse testes. Individual cells are color-coded according to their assigned cluster identities across 16 distinct cell states. Round spermatid stages comprise clusters S1, S3, S4, S6, and S7; elongating spermatid stages comprise clusters S9–S11. **C** Heatmap displaying the expression profiles of representative cluster-specific marker genes across the 16 identified cell populations. The color scale denotes z-score normalized expression levels. **D** Quantification and comparison of the proportional distribution of individual cell

subclusters between Ctrl and DKO testes.

Fig. 4 Defective spermiogenesis and ultrastructural abnormalities in DKO germ cells. A and **B** Gene Ontology (GO) enrichment terms for significantly down-regulated differentially expressed genes (DEGs) in DKO round spermatids (**A**) and elongating spermatids (**B**) compared with their respective controls. **C-F** Representative transmission electron microscopy (TEM) micrographs of cauda epididymal sperm and spermatids from Ctrl and DKO mice. **C** Cross-sections of sperm flagella showing axonemal disruptions (scale bar, 200 nm); **D** sperm heads displaying acrosomal defects (red arrow; scale bar, 200 nm); **E** disrupted head–tail coupling apparatus (red arrow; scale bar, 500 nm); and **F** vacuolated or disorganized mitochondrial architecture in the midpiece (red arrow; scale bar, 500 nm).

Fig. 5 Metabolic dysregulation and energy depletion in Tfeb/Tfe3-deficient testes. A Gene Ontology (GO) terms enriched among down-regulated DEGs in DKO Sertoli cells relative to Ctrl Sertoli cells. **B** Hierarchical clustering heatmap of significantly altered metabolites identified via untargeted metabolomics in Ctrl and DKO testis tissues. **C** Relative abundance box plots of key tricarboxylic acid (TCA) cycle intermediates: cis-aconitic acid, isocitric acid, fumaric acid, and L-malic acid. The whiskers indicate the minimum to maximum values. **D** Kyoto Encyclopedia of Genes and Genomes (KEGG) pathway analysis showing significantly enriched pathways among the down-regulated metabolites in DKO testes. **E** Total ATP concentration in whole testis lysates from Ctrl and DKO mice. Data are presented as mean ± s.e.m. $*P < 0.05$, $**P < 0.01$, $***P < 0.001$ by two-tailed Student's t-test.

Fig. 6 Tfeb and Tfe3 sustain mitochondrial function and directly transactivate Cycs. A Heatmap showing genome-wide Tfeb-binding intensities flanking peak centers determined by CUT&Tag sequencing (left) and corresponding functionally enriched GO terms for targeted loci (right). **B** Assessment of mitochondrial membrane potential (MMP) via JC-1 staining in primary Ctrl and DKO Sertoli cells. Red fluorescence indicates high MMP (JC-1 aggregates); green fluorescence indicates low MMP (JC-1 monomers). Scale bar, 5 μm. **C** Representative images of intracellular reactive oxygen species (ROS) levels detected by DCFH-DA fluorescent probing. Scale bar, 20 μm. **D** Immunoblot analysis of Cox4, Tomm20, and Cycs proteins in whole testis lysates from Ctrl and DKO mice. **E** Distribution of differential Tfeb CUT&Tag genomic binding signals and identified DEGs. Intersection numbers are indicated. **F** Genome-wide distribution of CUT&Tag peak intensities ranked by signal strength and plotted against

enrichment scores (log10-transformed). Representative target genes, including *Cycs*, *Atp5g2*, and *Atp5g3*, are highlighted. **G** Chromatin immunoprecipitation followed by quantitative PCR (ChIP–qPCR) analysis validating Tfeb occupancy at the *Cycs* promoter region. Normal rabbit IgG was used as a negative control (n = 3 independent biological replicates). Data are presented as mean ± s.e.m. *$p < 0.05$, **$p < 0.01$, ***$p < 0.001$ by two-tailed Student's t-test. **H** Dual-luciferase reporter activity in 293T cells co-transfected with plasmids expressing Tfeb, Tfe3, or an empty vector, alongside reporter constructs driven by either the wild-type (WT) *Cycs* promoter or promoters carrying mutations in predicted Tfeb/Tfe3 binding sites (M1, M2, M3, and a triple mutant). Data were normalized to Renilla luciferase activity (n = 3 independent biological replicates). All quantitative data are presented as mean ± s.e.m. *$P < 0.05$, **$P < 0.01$, ***$P < 0.001$ by one-way ANOVA followed by Tukey's post-hoc test.

Fig. 7 Tfeb/Tfe3-Cycs-ATP axis in Sertoli cells safeguards mitochondrial bioenergenetic homeostasis and male fertility.

Under physiological conditions, Tfeb and Tfe3 translocate into the nuclei of Sertoli cells, where they cooperatively drive the transcription of mitochondrial-respiration and bioenergetic genes, including *Cycs*. This transcriptional program maintains robust mitochondrial oxidative phosphorylation, ensuring adequate ATP generation and metabolic homeostasis. Stable energy output from Sertoli cells supports their critical architectural, nutritional, and phagocytic functions, which are required for germ cell differentiation, spermiogenesis, and sperm maturation. Conversely, upon *Amh-Cre*-mediated conditional ablation of *Tfeb* and *Tfe3*, the loss of direct transcriptional activation leads to a marked downregulation of *Cycs*, causing mitochondrial structural fragmentation, decreased membrane potential, excessive reactive oxygen species (ROS) accumulation, and severe ATP depletion. This bioenergetic collapse compromises the nursing capability of Sertoli cells, leading to comprehensive defects in spermatid remodeling and flagellar assembly, ultimately manifesting as oligo-astheno-teratozoospermia (OAT) and male infertility.

Fig. S1 Generation and fertility characterization of Sertoli cell-specific Tfeb conditional knockout mice. **A** Schematic diagram illustrating the targeting strategy for the conditional *Tfeb* floxed allele and *Amh-Cre*-mediated genomic excision. LoxP sites flank exons 1-7 of the *Tfeb*

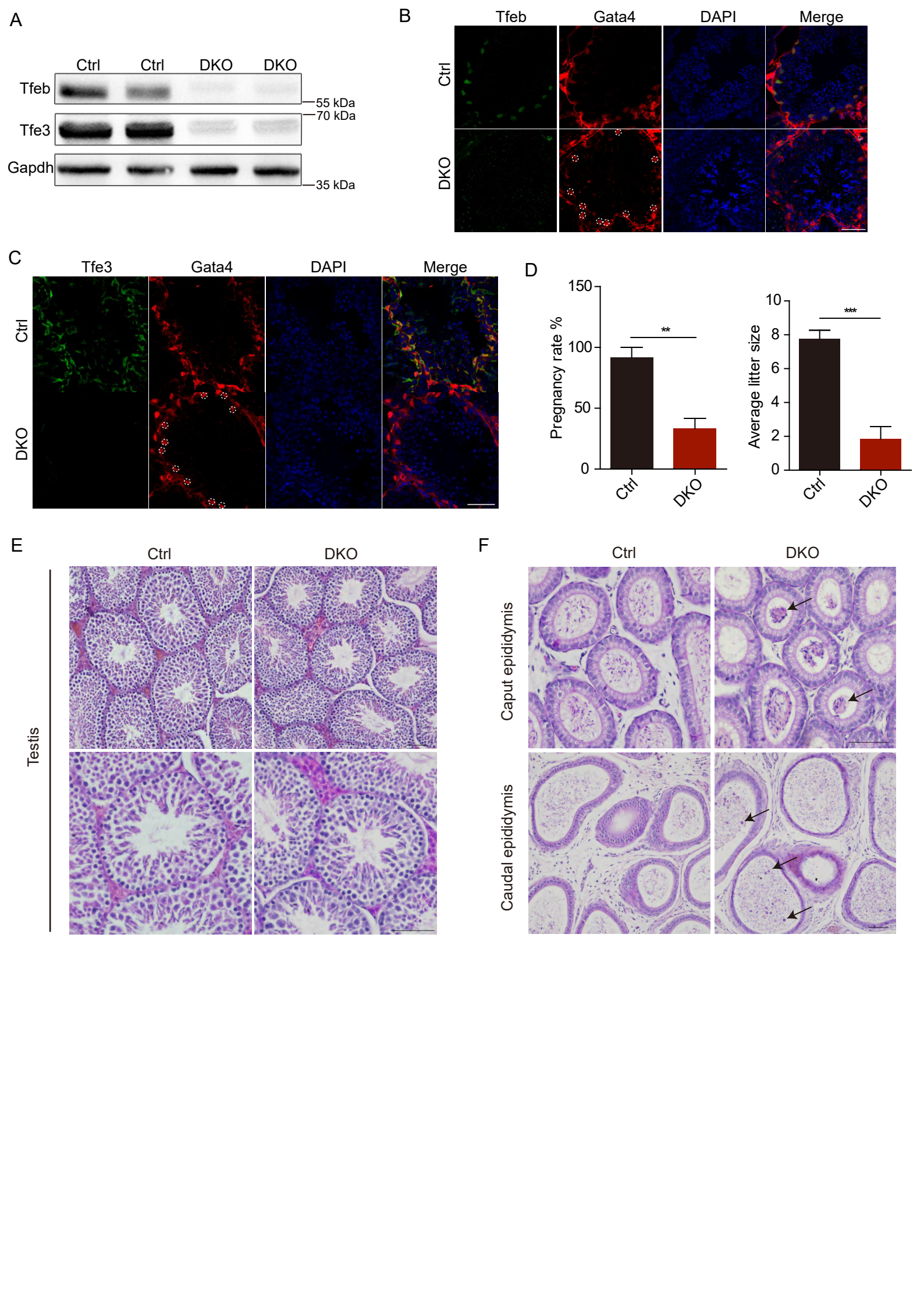
locus. **B** Immunoblot analysis of Tfeb protein expression in adult testis tissue lysates from control (Ctrl) and Sertoli cell-specific *Tfeb* conditional knockout mice. Gapdh was used as a loading control. Genotype definitions: Ctrl, $Tfeb^{fl/fl}$; $Tfeb^{cKO}$, *Amh-Cre*; $Tfeb^{fl/fl}$. **C** Immunofluorescence staining showing the expression and localization of Tfeb (green) in Ctrl and $Tfeb^{cKO}$ testis sections. Nuclei were counterstained with DAPI (blue). Scale bar, 50 μm. **D** Quantitative analysis of male fertility parameters, including pregnancy rates (left) and average litter sizes (right), from wild-type female mice vited with either Ctrl or $Tfeb^{cKO}$ males. Data are presented as mean ± s.e.m.; n.s., not significant by two-tailed Student's t-test. **E** Representative H&E staining of testis (top) and cauda epididymis (bottom) cross-sections from adult Ctrl and $Tfeb^{cKO}$ mice. Scale bar, 50 μm.

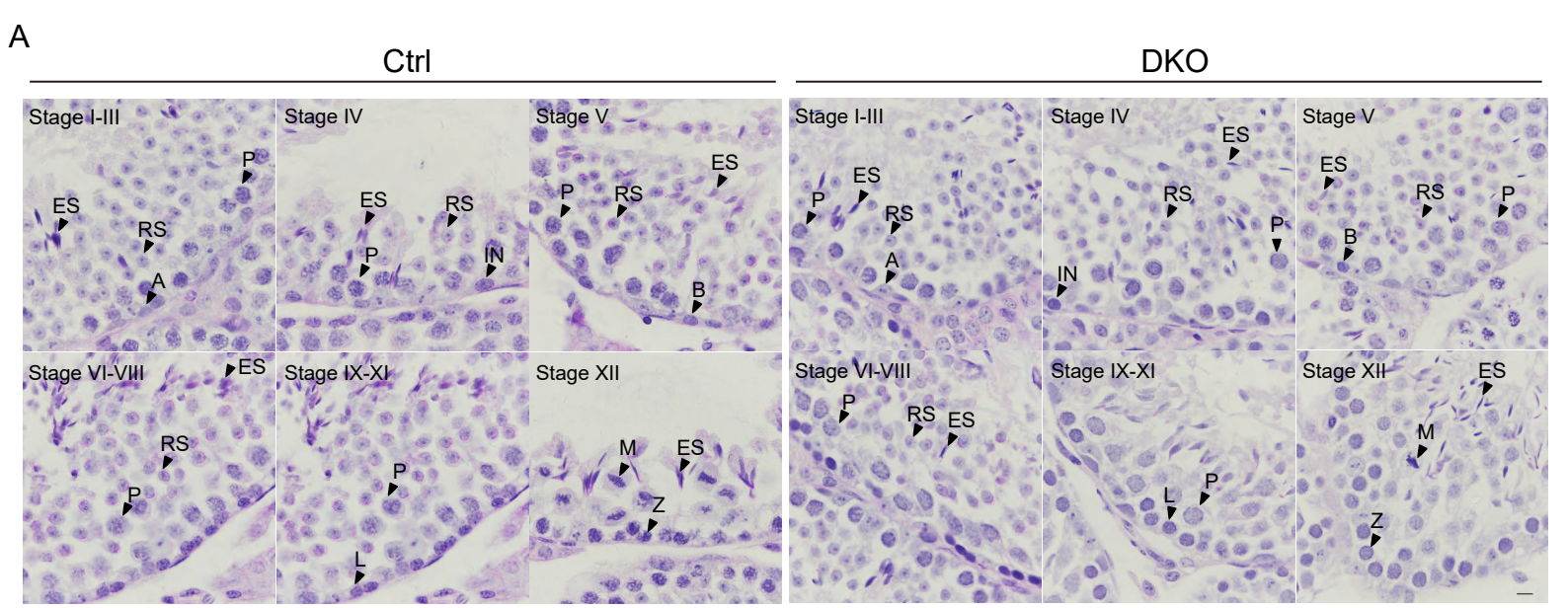
Fig. S2 Strategy for conditional ablation of Tfe3 in Sertoli cells and phenotypic evaluation. **A** Schematic of the mouse *Tfe3* gene targeting design. Diagramed are the wild-type locus, the floxed locus flanking exons 2-10 with loxP elements, and the truncated knockout sequence resulting from *Amh-Cre* recombination. ATG initiation site and exons are indicated. **B** Western blot analysis confirming the elimination of Tfe3 protein in $Tfe3^{cKO}$ testes compared with Ctrl lysates. Gapdh served as the loading control. Genotype definitions: Ctrl, $Tfe3^{fl/fl}$; $Tfe3^{cKO}$, *Amh-Cre*; $Tfe3^{fl/fl}$. **C** Immunofluorescence detection of Tfe3 (green) in adult Ctrl and $Tfe3^{cKO}$ testis sections, with DAPI (blue) counterstaining. Scale bar, 50 μm. **D** Reproductive performance metrics, including pregnancy rates and litter sizes, for Ctrl and $Tfe3^{cKO}$ male mice. Data are presented as mean ± s.e.m.; n.s., not significant by two-tailed Student's t-test. **E** H&E histological profiling of seminiferous tubules and epididymides from adult Ctrl and $Tfe3^{cKO}$ cohorts. Scale bar, 50 μm.

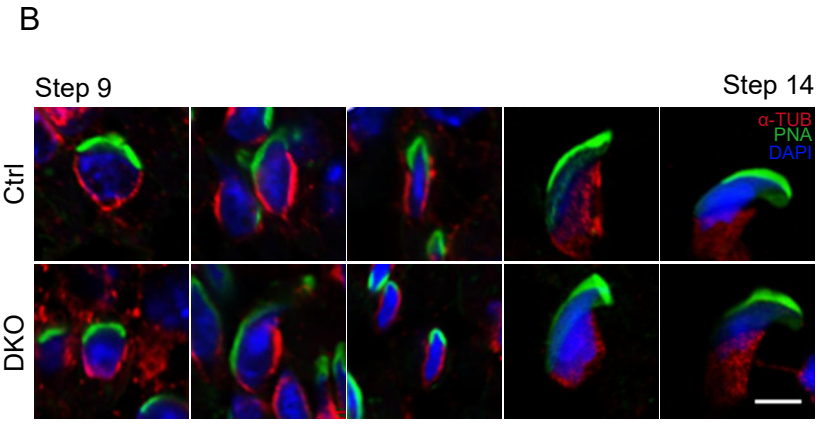
Fig. S3 Assessment of blood–testis barrier integrity and ultrastructure in DKO mice. A and **B** Representative immunofluorescence images of adult Ctrl and DKO testicular sections stained for MVH (green; germ cell marker), DAPI (blue), and either Tfeb (red, **A**) or Tfe3 (red, **B**). Scale bars, 50 μm. **C** High-magnification transmission electron microscopy (TEM) micrographs capturing the blood-testis barrier (BTB) tight junction complexes between adjacent Sertoli cells near the basement membrane in Ctrl and DKO testes. Sequential zoom-ins are displayed from left to right. Scale bars: 2 μm (left); 1 μm (middle); 500 nm (right).

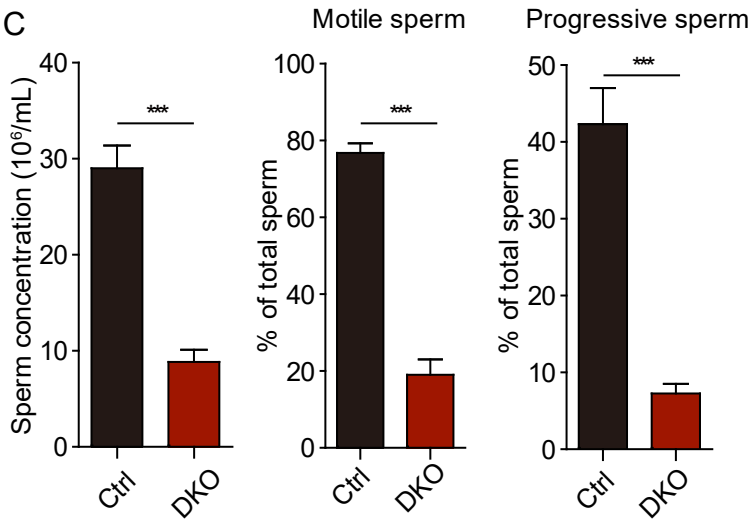
Fig. S4 Metabolomic profiling and functional decline in Tfeb and Tfe3 deficient Sertoli

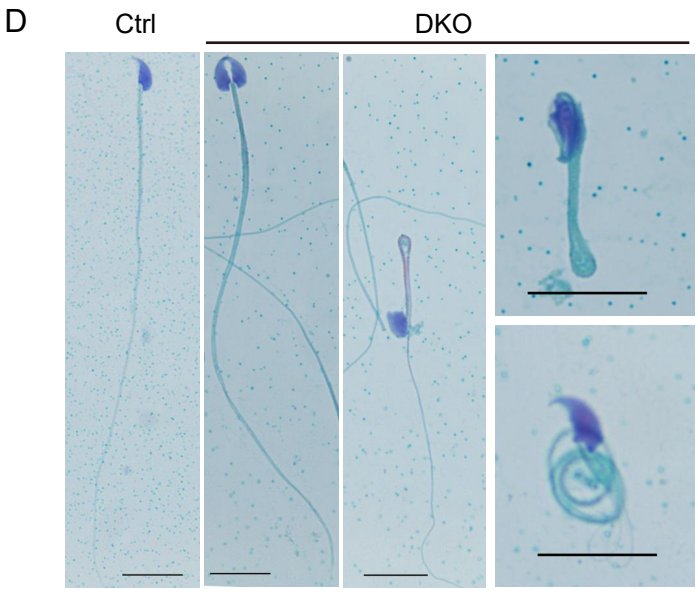
cells. A Principal Component Analysis (PCA) score plot based on untargeted metabolomics profiles from 8-week-old Ctrl and DKO testes (n = 7 independent biological replicates per group). **B** Immunofluorescence of primary Sertoli cells isolated from Ctrl and DKO mice, labeled with SOX9 (green) and counterstained with DAPI (blue). Scale bar, 10 μm. **C** Quantitative fluorometric ratio analysis of JC-1 (red/green signal intensity) confirming mitochondrial depolarization in DKO cells. Data are presented as mean ± s.e.m. ***$P < 0.01$ by two-tailed Student's t-test. **D** Quantitative measurement of cellular fluorometric intensity of total reactive oxygen species (ROS) production in Ctrl and DKO testis samples. Data are presented as mean ± s.e.m. ***$P < 0.001$ by two-tailed Student's t-test. **E** Densitometric quantification of relative protein abundances for Cycs, Tomm20, and Cox4 normalized to Gapdh levels from immunoblot replicates. Data are presented as mean ± s.e.m. *$P < 0.05$, **$P < 0.01$, ***$P < 0.001$ by two-tailed Student's t-test. **F** Representative Integrative Genomics Viewer (IGV) track visualization of Tfeb CUT&Tag alignment coverage signals at the *Cycs* genomic locus. Normal IgG track is aligned as the control background. **G** Schematic chart maps detailing the positional location of the specific upstream regulatory motifs (M1-M3) within the *Cycs* promoter cloned into downstream reporting assays.

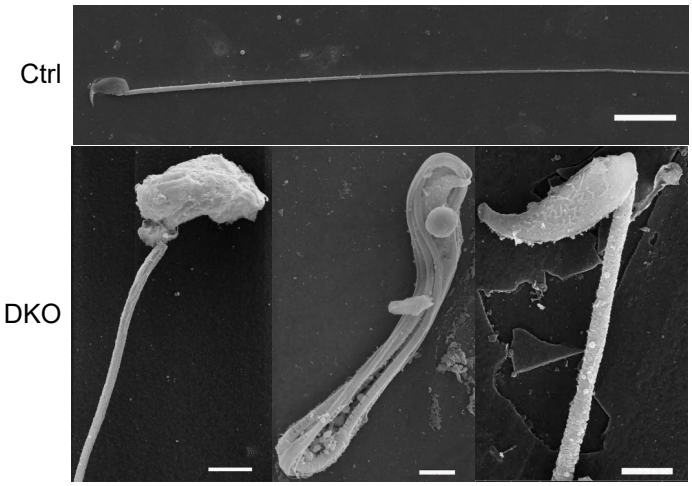

A
Ctrl
Ctrl
DKO
DKO
Tfeb
Tfe3
Gapdh
55 kDa
70 kDa
35 kDa
B
Tfeb
Gata4
DAPI
Merge
Ctrl
DKO
C
Tfe3
Gata4
DAPI
Merge
Ctrl
DKO
D
Pregnancy rate %
150
100
50
0
**
Ctrl
DKO
Average litter size
10
8
6
4
2
0
***
Ctrl
DKO
E
Ctrl
DKO
Testis
F
Ctrl
DKO
Caput epididymis
Caudal epididymis

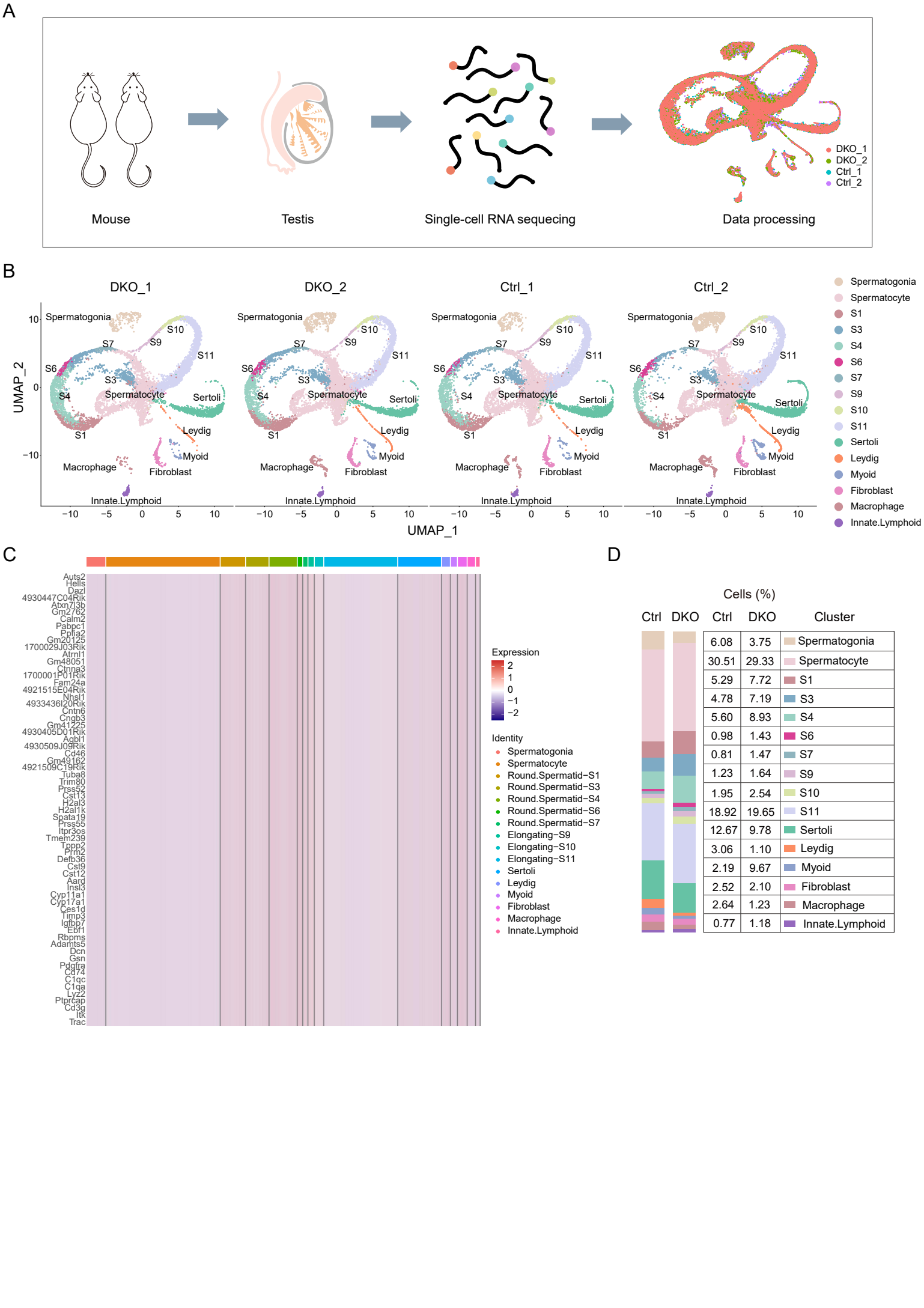

A
Ctrl
DKO
Stage I-III
Stage IV
Stage V
Stage VI-VIII
Stage IX-XI
Stage XII
P
ES
RS
A
IN
B
M
Z
L

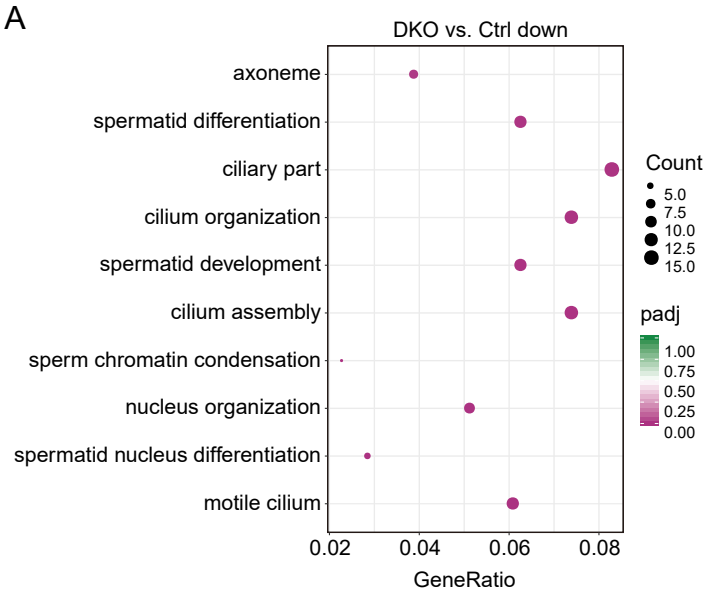

B
Step 9
Step 14
α-TUB
PNA
DAPI
Ctrl
DKO

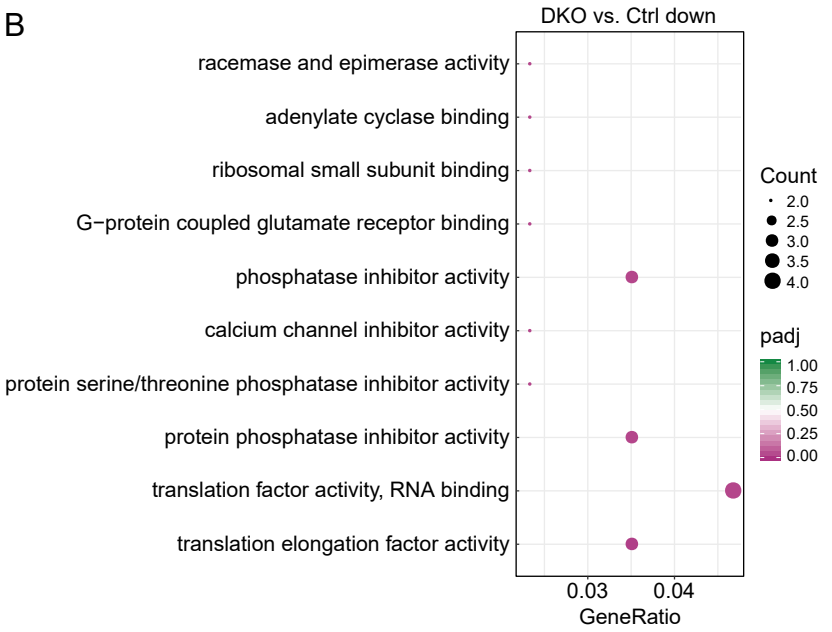

C
Motile sperm
Progressive sperm
Sperm concentration (10⁶/mL)
% of total sperm
% of total sperm
***
***
***
Ctrl
DKO
Ctrl
DKO
Ctrl
DKO

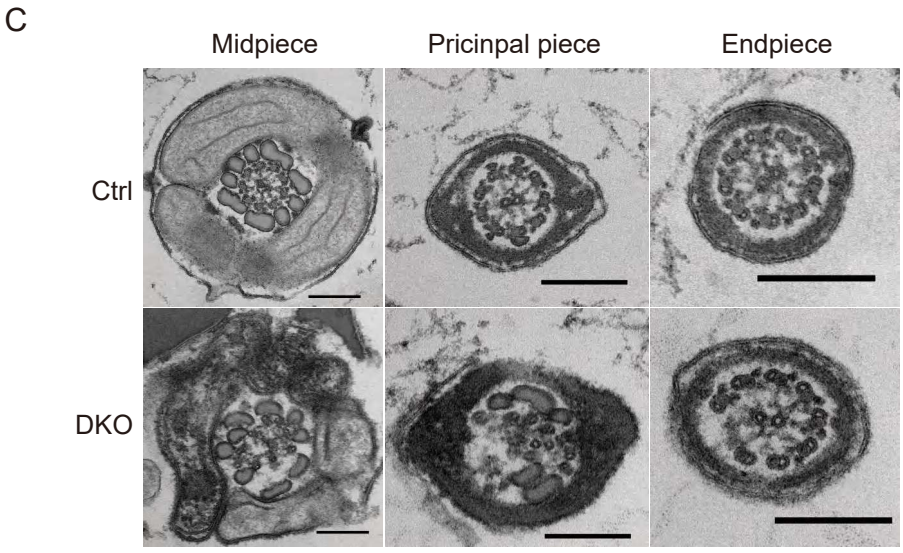

D
Ctrl
DKO

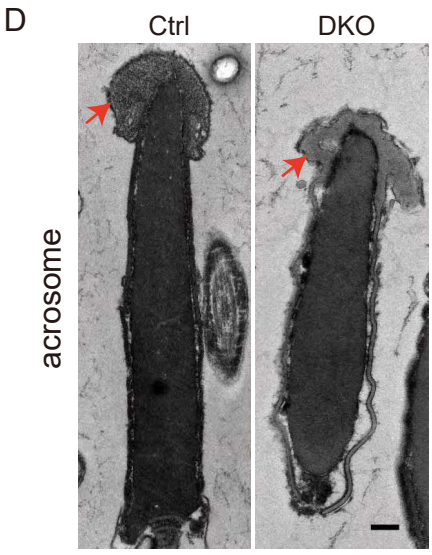

E
Ctrl
DKO

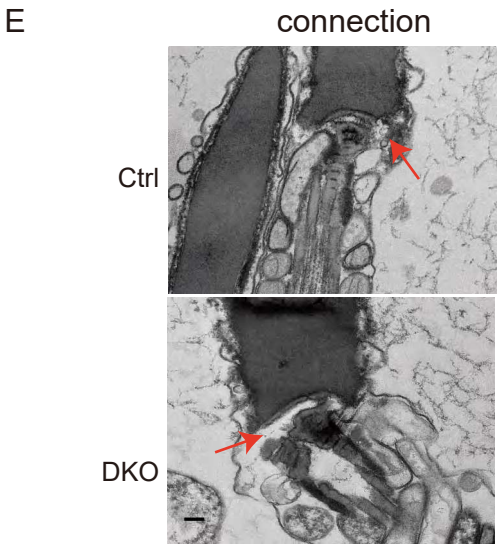

A
Mouse
Testis
Single-cell RNA sequecing
Data processing
DKO_1
DKO_2
Ctrl_1
Ctrl_2
B
DKO_1
DKO_2
Ctrl_1
Ctrl_2
UMAP_2
UMAP_1
Spermatogonia
Spermatocyte
S1
S3
S4
S6
S7
S9
S10
S11
Sertoli
Leydig
Myoid
Fibroblast
Macrophage
Innate.Lymphoid
C
Auts2
Hells
Dazl
4930447C04Rik
Atxn7l3b
Gm2762
Calm2
Pabpc1
Ppfia2
Gm20125
1700029J03Rik
Atml1
Gm48051
Ctnna3
1700001P01Rik
Fam24a
4921515E04Rik
Nhsl1
4933436I20Rik
Cntn6
Cngb3
Gm41225
4930405D01Rik
Agbl1
4930509J09Rik
Cd46
Gm49162
4921509C19Rik
Tuba8
Trim80
Prss42
Cst13
H2al3
H2al1k
Spata19
Prss55
Itpr3os
Tmem239
Tppp2
Prrn2
Defb36
Cst9
Cst12
Aard
Ins3
Cyp11a1
Cyp17a1
Ces1d
Timp3
Igfbp7
Ebf1
Rbpms
Adamts5
Dcn
Gsn
Pdgfra
Cd74
C1qc
C1qa
Lyz2
Ptprcap
Cd3g
Itk
Trac
Expression
2
1
0
−1
−2
Identity
Spermatogonia
Spermatocyte
Round.Spermatid−S1
Round.Spermatid−S3
Round.Spermatid−S4
Round.Spermatid−S6
Round.Spermatid−S7
Elongating−S9
Elongating−S10
Elongating−S11
Sertoli
Leydig
Myoid
Fibroblast
Macrophage
Innate.Lymphoid
D
Cells (%)
Ctrl
DKO
Ctrl
DKO
Cluster
6.08 3.75 Spermatogonia
30.51 29.33 Spermatocyte
5.29 7.72 S1
4.78 7.19 S3
5.60 8.93 S4
0.98 1.43 S6
0.81 1.47 S7
1.23 1.64 S9
1.95 2.54 S10
18.92 19.65 S11
12.67 9.78 Sertoli
3.06 1.10 Leydig
2.19 9.67 Myoid
2.52 2.10 Fibroblast
2.64 1.23 Macrophage
0.77 1.18 Innate.Lymphoid

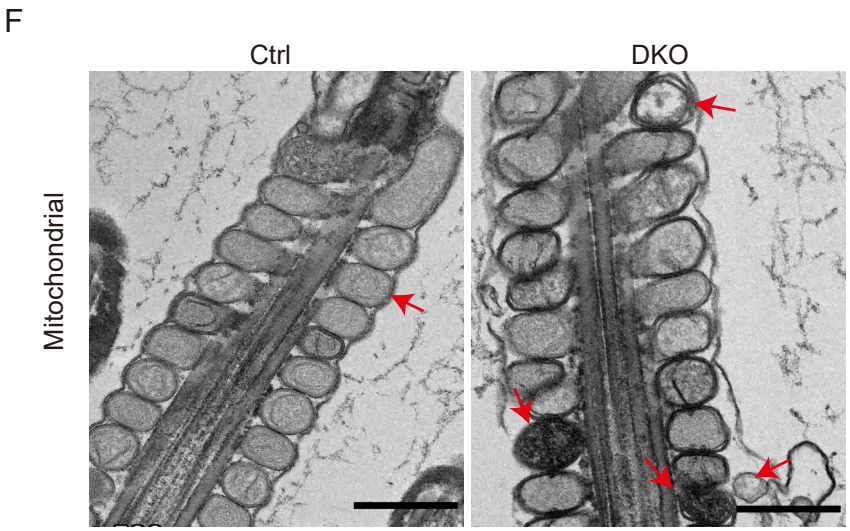

A
DKO vs. Ctrl down
axoneme
spermatid differentiation
ciliary part
cilium organization
spermatid development
cilium assembly
sperm chromatin condensation
nucleus organization
spermatid nucleus differentiation
motile cilium
0.02
0.04
0.06
0.08
GeneRatio
Count
5.0
7.5
10.0
12.5
15.0
padj
1.00
0.75
0.50
0.25
0.00

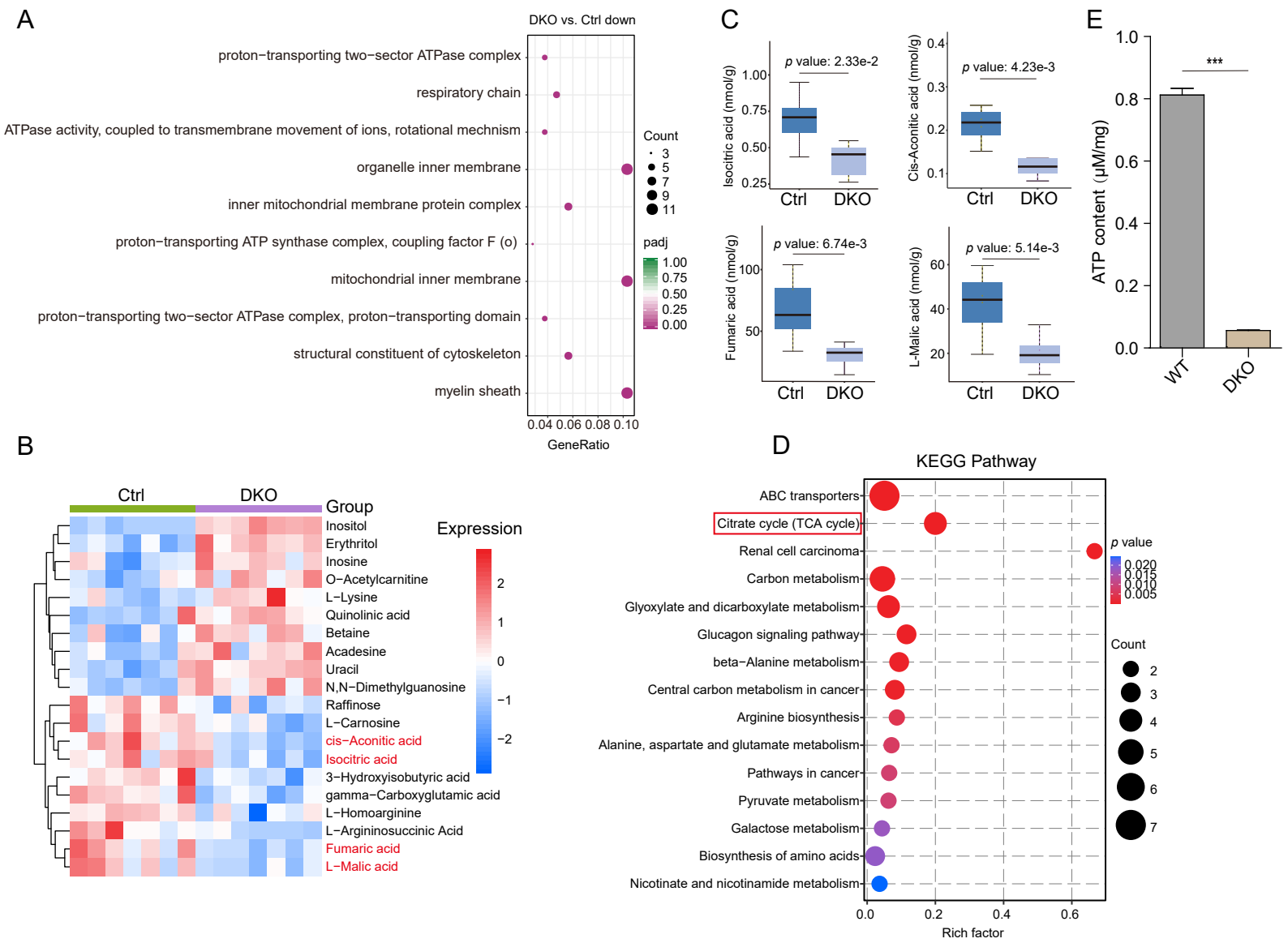

B
DKO vs. Ctrl down
racemase and epimerase activity
adenylate cyclase binding
ribosomal small subunit binding
G−protein coupled glutamate receptor binding
phosphatase inhibitor activity
calcium channel inhibitor activity
protein serine/threonine phosphatase inhibitor activity
protein phosphatase inhibitor activity
translation factor activity, RNA binding
translation elongation factor activity
0.03
0.04
GeneRatio
Count
2.0
2.5
3.0
3.5
4.0
padj
1.00
0.75
0.50
0.25
0.00

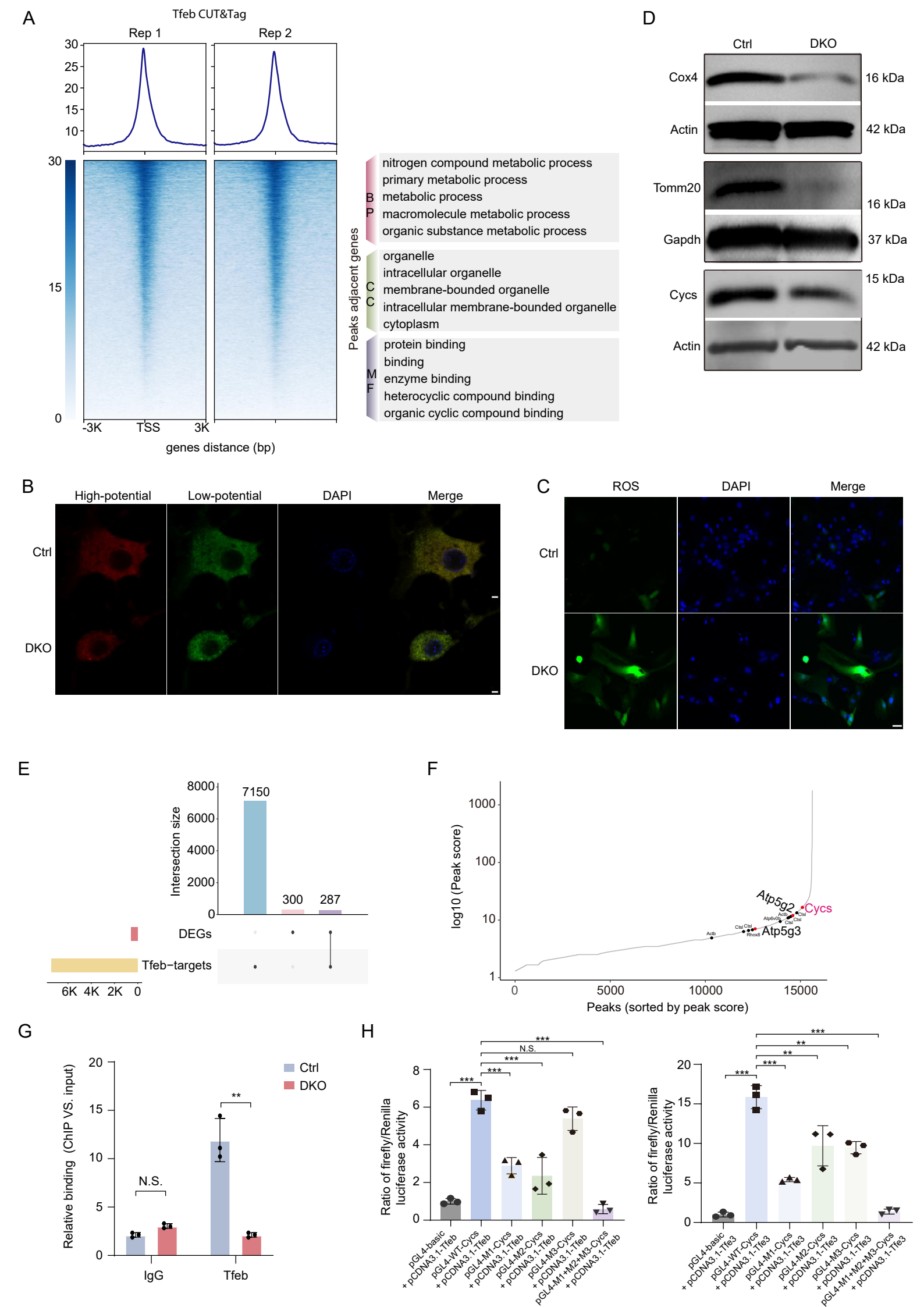

C
Midpiece
Pricinpal piece
Endpiece
Ctrl
DKO

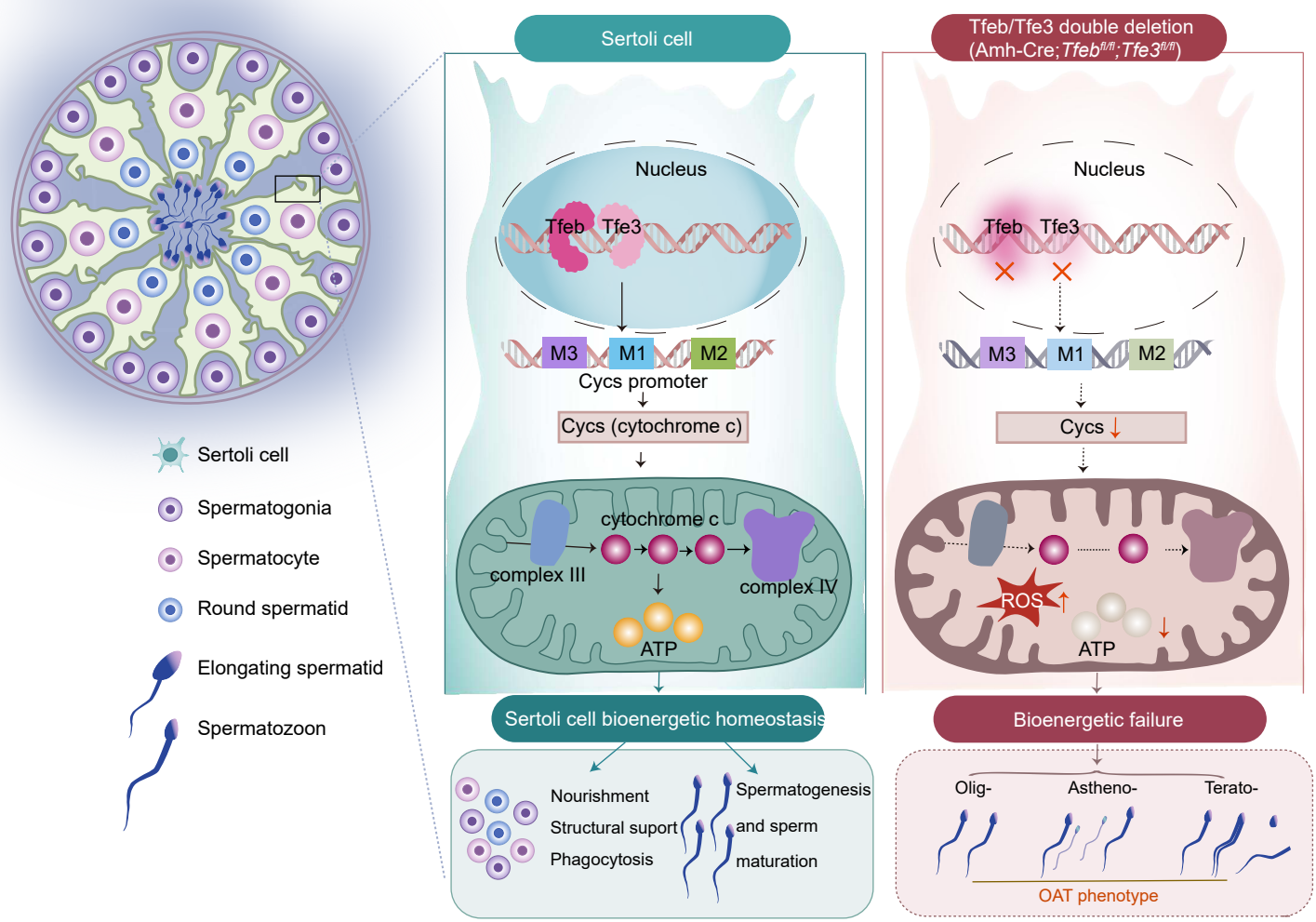

D
Ctrl
DKO
acrosome


E
connection
Ctrl
DKO


F
Ctrl
DKO
Mitochondrial


A
DKO vs. Ctrl down
proton−transporting two−sector ATPase complex
respiratory chain
ATPase activity, coupled to transmembrane movement of ions, rotational mechnism
organelle inner membrane
inner mitochondrial membrane protein complex
proton−transporting ATP synthase complex, coupling factor F (o)
mitochondrial inner membrane
proton−transporting two−sector ATPase complex, proton−transporting domain
structural constituent of cytoskeleton
myelin sheath
0.04 0.06 0.08 0.10
GeneRatio
Count
3
5
7
9
11
padj
1.00
0.75
0.50
0.25
0.00
C
p value: 2.33e-2
Isocitric acid (nmol/g)
Ctrl
DKO
p value: 4.23e-3
Cis-Aconitic acid (nmol/g)
p value: 6.74e-3
Fumaric acid (nmol/g)
p value: 5.14e-3
L-Malic acid (nmol/g)
E
***
ATP content (μM/mg)
WT
DKO
B
Ctrl
DKO
Group
Expression
Inositol
Erythritol
Inosine
O−Acetylcarnitine
L−Lysine
Quinolinic acid
Betaine
Acadesine
Uracil
N,N−Dimethylguanosine
Raffinose
L−Carnosine
cis−Aconitic acid
Isocitric acid
3−Hydroxyisobutyric acid
gamma−Carboxyglutamic acid
L−Homoarginine
L−Argininosuccinic Acid
Fumaric acid
L−Malic acid
D
KEGG Pathway
ABC transporters
Citrate cycle (TCA cycle)
Renal cell carcinoma
Carbon metabolism
Glyoxylate and dicarboxylate metabolism
Glucagon signaling pathway
beta−Alanine metabolism
Central carbon metabolism in cancer
Arginine biosynthesis
Alanine, aspartate and glutamate metabolism
Pathways in cancer
Pyruvate metabolism
Galactose metabolism
Biosynthesis of amino acids
Nicotinate and nicotinamide metabolism
Rich factor
p value
Count


A
Tfeb CUT&Tag
Rep 1
Rep 2
30
25
20
15
10
30
15
0
-3K
TSS
3K
genes distance (bp)
Peaks adjacent genes
BP
nitrogen compound metabolic process
primary metabolic process
metabolic process
macromolecule metabolic process
organic substance metabolic process
CC
organelle
intracellular organelle
membrane-bounded organelle
intracellular membrane-bounded organelle
cytoplasm
MF
protein binding
binding
enzyme binding
heterocyclic compound binding
organic cyclic compound binding
D
Ctrl
DKO
Cox4
16 kDa
Actin
42 kDa
Tomm20
16 kDa
Gapdh
37 kDa
Cycs
15 kDa
Actin
42 kDa
B
High-potential
Low-potential
DAPI
Merge
Ctrl
DKO
C
ROS
DAPI
Merge
Ctrl
DKO
E
Intersection size
8000
6000
4000
2000
0
7150
300
287
DEGs
Tfeb−targets
6K 4K 2K 0
F
log10 (Peak score)
1000
100
10
1
0
5000
10000
15000
Peaks (sorted by peak score)
Atp5g2
Cycs
Atp5g3
G
Relative binding (ChIP VS. input)
20
15
10
5
0
Ctrl
DKO
N.S.
**
IgG
Tfeb
H
Ratio of firefly/Renilla luciferase activity
8
6
4
2
0
***
N.S.
***
***
***
pGL4-basic + pCDNA3.1-Tfeb
pGL4-WT-Cycs + pCDNA3.1-Tfeb
pGL4-M1-Cycs + pCDNA3.1-Tfeb
pGL4-M2-Cycs + pCDNA3.1-Tfeb
pGL4-M3-Cycs + pCDNA3.1-Tfeb
pGL4-M1+M2+M3-Cycs + pCDNA3.1-Tfeb
Ratio of firefly/Renilla luciferase activity
20
15
10
5
0
***
**
**
***
***
pGL4-basic + pCDNA3.1-Tfe3
pGL4-WT-Cycs + pCDNA3.1-Tfe3
pGL4-M1-Cycs + pCDNA3.1-Tfe3
pGL4-M2-Cycs + pCDNA3.1-Tfe3
pGL4-M3-Cycs + pCDNA3.1-Tfe3
pGL4-M1+M2+M3-Cycs + pCDNA3.1-Tfe3


Sertoli cell
Spermatogonia
Spermatocyte
Round spermatid
Elongating spermatid
Spermatozoon
Sertoli cell
Nucleus
Tfeb
Tfe3
M3
M1
M2
Cycs promoter
Cycs (cytochrome c)
cytochrome c
complex III
complex IV
ATP
Sertoli cell bioenergetic homeostasis
Nourishment
Structural suport
Phagocytosis
Spermatogenesis
and sperm
maturation
Tfeb/Tfe3 double deletion
(Amh-Cre;Tfeb^fl/fl;Tfe3^fl/fl)
Nucleus
Tfeb
Tfe3
M3
M1
M2
Cycs ↓
ROS
ATP
Bioenergetic failure
Olig-
Astheno-
Terato-
OAT phenotype

Supplementary Files

This is a list of supplementary files associated with this preprint. Click to download.

- TableS2.xlsx
- TableS1.xlsx
- Supplementaryfigures.docx